Mon. Not. R. Astron. Soc. 347, 740–758 (2004)

GRAPE-SPH chemodynamical simulation of elliptical galaxies – I. Evolution of metallicity gradients

Chiaki Kobayashi*
Max-Planck-Institute for Astrophysics, Karl-Schwarzschild-Str. 1, D-85741 Garching, Germany

Accepted 2003 October 3. Received 2003 October 1; in original form 2003 March 4

ABSTRACT

We simulate the formation and chemodynamical evolution of 124 elliptical galaxies using a GRAPE-SPH code that includes various physical processes that are associated with the formation of stellar systems: radiative cooling, star formation, feedback from Type II and Ia supernovae and stellar winds, and chemical enrichment. In our cold dark matter (CDM)-based scenario, galaxies form through the successive merging of subgalaxies with various masses. Their merging histories vary between a major merger at one extreme and a monolithic collapse of a slow-rotating gas cloud at the other extreme. We examine the physical conditions during 151 merging events that occur in our simulation. The basic processes driving the evolution of the metallicity gradients are as follows: (i) destruction by mergers to an extent dependent on the progenitor mass ratio; (ii) regeneration when strong central star formation is induced at a rate dependent on the gas mass of the secondary; and (iii) slow evolution as star formation is induced in the outer regions through late gas accretion. We succeed in reproducing the observed variety of the radial metallicity gradients. The average metallicity gradient $\Delta\log Z/\Delta\log r \simeq -0.3$ with dispersion of ± 0.2 and no correlation between gradient and galaxy mass are consistent with observations of Mg_2 gradients. The variety of the gradients stems from the difference in the merging histories. Galaxies that form monolithically have steeper gradients, while galaxies that undergo major mergers have shallower gradients. Thus merging histories can, in principle, be inferred from the observed metallicity gradients of present-day galaxies. The observed variation in the metallicity gradients cannot be explained either by *monolithic collapse* or by *major merger* alone. Rather it requires a model in which both formation processes arise, such as the present CDM scheme.

Key words: methods: *N*-body simulations – galaxies: abundances – galaxies: elliptical and lenticular, cD – galaxies: evolution – galaxies: formation.

1 INTRODUCTION

The internal structure of galaxies, spectrophotometric, chemical and dynamical properties of various locations within a galaxy, is closely related to the processes of galaxy formation and evolution. Stars in a galaxy are fossils; the star formation and chemical enrichment history of the galaxy are imprinted on their kinematics and chemical abundances. The SAURON project with the William Herschel Telescope (Bacon et al. 2001) is providing the wide-field mapping of the kinematics and stellar population, which will certainly give stringent constraints on the galaxy formation and evolution. Multi-object and integral field spectrographs are being developed also on 8–10 m ground-based telescopes, which can give the time evolution of such internal structure. To derive the physical processes from such observational data, it is necessary to construct a realistic model, i.e. a three-dimensional chemodynamical model, and to compare the theoretical predictions with such observational data.

Theoretical approaches have been performed in many ways. (i) The one-zone model (e.g. Tinsley 1980; Arimoto & Yoshii 1987; Matteucci 1996) played an important role in constructing the basic evolutionary scenarios of galaxies. In this model, the star formation history of a galaxy is constructed by carefully comparing the model predictions with the mean photometric and chemical properties of observed galaxies. However, because of the simplified assumption that all matter in a galaxy is well-mixed instantaneously, the one-zone model provides no idea of the internal structure of galaxies. (ii) The semi-analytic model (e.g. Kauffmann, White & Guiderdoni 1993; Cole et al. 1994), which is based on the Press–Schechter theory, can provide the mass function of dark haloes, their survival time-scales and the merging rates. By adopting empirical laws to determine the stellar mass and the mass of heavy elements, and by

*E-mail: chiaki@MPA-Garching.MPG.DE

© 2004 RAS

introducing simple rules to determine the galaxy morphology (i.e. an elliptical galaxy forms from the major merger of spiral galaxies), the semi-analytic model could reproduce some correlations among global properties (e.g. the Tully–Fisher relation and colour–magnitude relation) and some constraints on the number of galaxies (e.g. the luminosity function and number counts). However, there seems to be some difficulty in explaining the number evolution of elliptical galaxies (e.g. Benson, Ellis & Menanteau 2002). The observed information on the internal structures remains untouched. (iii) Numerical simulations of dissipationless systems (e.g. Toomre & Toomre 1972; White 1978) provide the interpretation of the interaction of galaxies and the internal structure of a galaxy. The gas dynamics in three dimensions was included in such numerical simulations (e.g. Hernquist & Katz 1989), and then star formation, feedback (Katz 1992) and chemical enrichment (Steinmetz & Müller 1994) were included. It is now possible to predict the spatial distributions of gas, stars and heavy elements in a galaxy. However, a comparison with observations has not been fully attempted yet. The reason is that it takes a long time to calculate the evolution of one galaxy with enough resolution to predict such distributions. To reduce the calculation time and to improve the resolution, a variety of methods have been invented.

The smoothed particle hydrodynamics (SPH) method is widely used to calculate three dimensional hydrodynamics with a Lagrangian scheme (Gingold & Monaghan 1977; Lucy 1977; Monaghan 1992 for a review), and has been applied to many astrophysical problems that have large density contrasts; formation of galaxies (Hernquist & Katz 1989; Navarro & White 1993; Steinmetz & Müller 1994) and a cloud–cloud collision (Lattanzio et al. 1985; Habe & Ohta 1992). Various codes have been developed to combine SPH with collisionless particles (i.e. dark matter and star particles; hereafter an N-body system) using different methods to calculate gravitational forces; direct summations, particle–particle/particle–mesh methods (Evrard 1988), tree methods (Hernquist & Katz 1989; Benz et al. 1990) and the method using the special purpose computer GRAPE (Gravity Pipe) (Umemura et al. 1993; Steinmetz 1996). GRAPE is a special purpose computer for efficiently calculating gravitational force and potential (Sugimoto et al. 1990). The GRAPE-SPH enables us to simulate the formation and evolution of a galaxy with more than 10^4 particles in as short a calculation time as a few days. It makes it possible to simulate many types of galaxies with different initial conditions, which is crucial for studying the formation and evolution of galaxies statistically.

The aim of our study is to put constraints on the formation history of elliptical galaxies by comparing the observed internal structures of stellar population. To construct a self-consistent three-dimensional chemodynamical model, we have introduced various physical processes associated with the formation of stellar systems such as radiative cooling, star formation, feedback of Type II and Ia supernovae (SNe II and SNe Ia), and stellar winds (SWs), and chemical enrichment. The chemical enrichment of SNe Ia has recently been included in several chemodynamical models. Among the two alternative scenarios for the SN Ia progenitor (e.g. Kobayashi et al. 1998), most chemodynamical models (Raiteri, Villata & Navarro 1996; Carraro, Lia & Chiosi 1998) adopted Greggio & Renzini's (1983) formulation based on the double-degenerate scenario. Mosconi et al. (2001) adopted single-time delay for the SN Ia contribution, and the parameter corresponds to the double-degenerate scenario. The single-degenerate scenario was introduced in Nakasato & Nomoto (2003) and Kawata & Gibson (2003). It may be useful to note that Woosley & Weaver's (1995) iron yield is too large compared with the observed abundance ratios in the Milky Way Galaxy, and thus their iron yield should be reduced to be half. Such a modification is always adopted in the one-zone models, but is never mentioned in many chemodynamical models. We have constructed a realistic model of chemical enrichment, excluding the instantaneous recycling approximation, including the mass-dependent yields of SNe II and the single-degenerate scenario of SNe Ia. We then solved the evolution of slowly rotating systems that consist of dark matter, gas and stars from various initial conditions to predict the spatial distribution of stellar population within a galaxy. By comparing the theoretical metallicity gradients with the observed ones, we discuss the origin of elliptical galaxies.

How elliptical galaxies form is a long-standing matter of big debate. The regularity in the light distribution and the global velocity anisotropy in elliptical galaxies were explained by the violent relaxation (Lynden-Bell 1967). Effectively dissipationless formation of an elliptical galaxy was discussed in various ways; e.g. stars have formed prior to the beginning of the collapse of the gas cloud (Gott 1973, 1975) or stars have formed slowly in disc galaxies, which subsequently merge to make a spheroidal galaxy (Marchant & Shapiro 1977; Toomre 1977; Barnes 1988). The limit of completely dissipationless collapse is amenable to N-body experiments, which can form the objects that have the observed dynamical properties. However, the dissipation during the formation is indispensable to explain the photometric and chemical properties of elliptical galaxies such as the colour–magnitude relation, the mass–metallicity relation and the radial metallicity gradients.

Two competing scenarios of the formation of elliptical galaxies have so far been proposed: elliptical galaxies should form monolithically by the gravitational collapse of a gas cloud with considerable energy dissipation (hereafter referred to as the monolithic collapse hypothesis; e.g. Larson 1974b; Arimoto & Yoshii 1987), or alternatively ellipticals should form via mergers of gaseous disc galaxies or of many dwarf galaxies (hereafter referred to as the merger hypothesis; e.g. Toomre 1977; Kauffmann et al. 1993; Baugh, Cole & Frenk 1996; Steinmetz & Navarro 2002). The merger hypothesis can be supported by the dynamical disturbances of observed ellipticals such as shells/ripples and multiple cores (Schweizer et al. 1990; Schweizer & Seitzer 1992; see also Bender & Surma 1992), and may easily explain the morphology–density relation of galaxies in clusters (Dressler 1980; Dressler et al. 1997). However, elliptical galaxies apparently show little evidence for on-going star formation, the bulk of their stars are old (e.g. Kodama & Arimoto 1997; Kodama et al. 1998; Silva & Bothun 1998; Stanford, Eisenhardt & Dickinson 1998). The monolithic collapse hypothesis assumes that the bulk of stars in ellipticals form during an initial starburst at high redshift, and that the star formation is terminated by a supernovae-driven galactic wind that expels the left-over interstellar gas from galaxies. The galactic wind is supposed to play an essential role in injecting heavy elements into the hot intracluster gas (Ciotti et al. 1991) and predicts tight correlations among global properties of galaxies such as the colour–magnitude relation (Bower, Lucey & Ellis 1992), the metallicity–velocity dispersion relation (Davies et al. 1987) and the fundamental plane (Djorgovski & Davis 1987; Dressler et al. 1987). [The colour–magnitude relation could be reproduced also under the merger hypothesis (Kauffmann & Charlot 1998, but see Cole et al. 2000).] Recent observations of clusters at high redshifts reveal that these relationships exist even at $z \sim 1$ (Dickinson 1996; Kelson et al. 1997; Schade, Barrientos & Lopez-Cruz 1997; Stanford et al. 1998), which indicates that the bulk of stars in cluster ellipticals form at the redshift $z_f \gtrsim 2.5$–4 (Kodama et al. 1998).

However, for cluster early-type galaxies, it has been argued that the 'progenitor bias' is significant; the progenitors of the youngest

low-redshift, early-type galaxies drop out of the sample at high redshift (Kauffmann 1996; van Dokkum & Franx 1996, 2001). Thus the evolution of field early-type galaxies is now paid attention as the observational constraints. Franceschini et al. (1998) found that HDF-N early-type galaxies are relatively young with the formation epochs spanning $1 \lesssim z \lesssim 4$, but no evolution of field elliptical galaxies found at least $z \lesssim 1$ (Schade et al. 1999; Brinchmann & Ellis 2000; Im et al. 2002; see also Daddi, Cimatti & Renzini 2000). Drory et al. (2001) found mass evolution at $0.4 < z < 1.2$. At high redshift, the number of field red ellipticals is smaller than expected by the monolithic collapse hypothesis (Zepf 1997; Menanteau et al. 1999; Bargar et al. 1999) and there may be some global evolution that is consistent with the hierarchical clustering scenario (Fontana et al. 1999; Dickinson et al. 2003; but see Cimatti et al. 2002).

The radial metallicity gradient gives one of the most stringent constraints on the galaxy formation. Numerical simulations of the collapse of galaxies including star formation definitely predict strong radial gradients in chemical enrichment (e.g. Larson 1974a, 1975; Carlberg 1984), whereas the dissipationless collapse models predict no gradient in chemical enrichment (Gott 1973, 1975). During the collapse, gas is chemically enriched, flows inward and forms new stars, which form the radial metallicity gradients. The metallicity gradients are observed as radial gradients of colours and spectral line indices (e.g. Faber 1973, 1977; Davies, Sadler & Peletier 1993; Kobayashi & Arimoto 1999 for a review). A typical observed metallicity gradient of elliptical galaxies is $\Delta \log Z / \Delta \log r \simeq -0.3$, which is less steep than those predicted by numerical simulations of dissipative collapse (-0.35 in Larson 1974a; -1.0 in Larson 1975; -0.5 in Carlberg 1984). Furthermore, if elliptical galaxies form monolithically from a massive gas cloud, the metallicity gradient should correlate with the global properties of galaxies in the sense that more massive galaxies have steeper gradients (Carlberg 1984).

The observational feature of metallicity gradients is complicated and confusing because of a lack of suitable samples of uniform quality. It was shown that elliptical galaxies with larger values of the central Mg_2 ($\sim$5100 Å) index tend to have steeper Mg_2 gradients (Gorgas, Efstathiou & Aragón-Salamanca 1990; Carollo, Danziger & Buson 1993; Gonzalez & Gorgas 1996). However, Davies et al. (1993) did not find any significant correlation between the Mg_2 gradient and σ_0 in a sample of 13 galaxies. Kobayashi & Arimoto (1999) restudied line-strength gradients of 80 elliptical galaxies using the indices of Mg_2, Mg_b (5177 Å), Fe_1 (5270 Å), Fe_2 (5335 Å) and Hβ (4861 Å), and found that the metallicity gradients do not correlate with any physical properties of galaxies, including central and mean metallicities, central velocity dispersions, absolute B-magnitudes, absolute effective radii and dynamical masses of galaxies. Elliptical galaxies have different metallicity gradients, even if they have nearly identical properties such as masses, luminosities and metallicities.

This discrepancy could be solved if mergers flatten the original gradient. Indeed, numerical simulations showed that the gradient in a disc galaxy should be halved after three successive mergers of galaxies with similar size (White 1980). However, according to the dissipationless N-body experiment, the initial state is not fully wiped out during the violent relaxation phase and N-body particles that were in the outer region of a progenitor galaxy are found in a similar location after merging events (van Albada 1982). From this point, it has been mentioned that the metallicity gradient is not reduced by a merger (e.g. Barnes 1996). Simulations of both dissipative collapse and mergers leave room for improvement, because essential physical processes such as star formation, feedback of supernovae and metal enrichment were not taken into account.

Here we simulate the chemodynamical evolution of elliptical galaxies based on the cold dark matter (CDM) picture. In CDM cosmology, the amplitude of primordial fluctuation decreases with increasing wavelength, and the formation of structure is driven by the hierarchical clustering. Galaxies should form through the successive mergings of subgalaxies with various masses. In contrast with the semi-analytic models, we exclude the assumption that elliptical galaxies form only from the major merger of disc galaxies. Instead we allow various merging histories for elliptical galaxies. In some cases, an elliptical galaxy forms by an assembly of gas rich small galaxies, which looks like a monolithic collapse. In other cases, the evolved galaxies with little gas merge to form an elliptical galaxy. This scenario is the middle way between monolithic collapse and major merger of disc galaxies.

In this paper, we first describe the GRAPE-SPH code and the modelling of physical processes (Section 2). We classify simulated galaxies according to their merging histories (Section 3.1) and derive the present metallicity gradients (Section 3.2). In Section 3.3, we show that the scatter of the metallicity gradients comes from the difference in merging histories and discuss the origin of elliptical galaxies by comparing with the observations. In Section 3.4, we examine the evolution of metallicity gradients via merging events that occur in our simulation, and manifest the dependences on mass ratios of merging galaxies, gas fractions and induced star formation. In Section 4, we mention some future works and possible problems, our conclusions are given in Section 5.

2 CHEMODYNAMICAL MODEL

2.1 Hydrodynamics

Here we describe the GRAPE-SPH code, which was originally written by Nakasato (2000), and is highly adaptive in space and time by means of individual smoothing lengths and individual time-steps. The SPH formulation used in the code is almost the same as Navarro & White (1993).

Instead of the continuity equation, the density ρ of each particle is determined from

$$\langle \rho(\boldsymbol{r}_i) \rangle = \rho_i = \sum m_j W(r, h). \tag{1}$$

where r is defined as $r = |\boldsymbol{r}_i - \boldsymbol{r}_j|$, and h denotes the symmetrized smoothing length defined as $h = h_{ij} = \frac{1}{2}(h_i + h_j)$. The momentum equation is represented as

$$\frac{D\boldsymbol{v}_i}{Dt} = -\sum m_j \left(\frac{P_i}{\rho_i^2} + \frac{P_j}{\rho_j^2} + \Pi_{ij} \right) \nabla_i W(r, h) - (\nabla \Phi)_i. \tag{2}$$

The energy equation is represented as

$$\frac{Du_i}{Dt} = -\sum m_j \left(\frac{P_i}{\rho_i^2} + \frac{1}{2}\Pi_{ij} \right) (\boldsymbol{v}_i - \boldsymbol{v}_j) \cdot \nabla_i W(r, h) + \frac{\mathcal{H}_i - \Lambda_i}{\rho_i}. \tag{3}$$

where thermal conduction is neglected. We also use the equation of state for an ideal gas with $\gamma = \frac{5}{3}$;

$$P_i = (\gamma - 1)\rho_i u_i. \tag{4}$$

The smoothing length h varies spatially, evolves with time and is computed for each particle in every time-step. For the kernel W, a spherically symmetric spline (Monaghan & Lattanzio 1985; Monaghan 1992) is adopted. For the derivative of the kernel ∇W, the revised form by Thomas & Couchman (1992) is adopted. For the artificial viscous term Π_{ij}, we use the modified Monaghan &

Gingold (1983) tensor and the shear-free viscosity formulation with $\alpha = 1.0$ and $\beta = 2.0$ (Balsara 1995; Navarro & Steinmetz 1997). The heating $\mathcal{H}$ and cooling Λ rates are described in the following subsection.

In the SPH code, a gas particle interacts with dark matter and star particles only by gravity. The gravitational potential Φ is given as

$$\Phi(\boldsymbol{r}_i) = -G \sum \frac{m_j}{\sqrt{|\boldsymbol{r}_i - \boldsymbol{r}_j|^2 + \epsilon^2}}, \tag{5}$$

where G is the gravitational constant. ϵ is the gravitational softening length, which we set $\epsilon = 0.5$ and 1.0 kpc for the high- and low-resolution, respectively. The gravity between these particles is calculated in direct summation using the GRAPE5 MUV (Mitaka Underground Vineyard) system in the National Astronomical Observatory of Japan and GRAPE6 of the University of Tokyo.

We use an individual time-step scheme with the following two steps. First, we compute the time-step of each particle Δt_i from the dynamical criteria using the velocity v and the acceleration a (Katz, Weinberg & Hernquist 1996); Δt_i is the minimum of $\eta^2 \epsilon/|v|$ and $\eta\sqrt{\epsilon/|a|}$, where η is a numerical parameter, and is set to be $\eta = 0.5$. Then, we derive the actual time-step Δt_n from the greatest power of 2 subdivision of the system time-step $\Delta t_{\rm sys}$, which is smaller than Δt_i; $\Delta t_n = \Delta t_{\rm sys}/2^n \leqslant \Delta t_i$ (Navarro & White 1993). The system time-step is a fundamental time-step used to synchronize all particles, and is set to be $\Delta t_{\rm sys} = 2$ Myr. The time integration of the equation of motion is performed using a leap-frog method modified for the individual time-step scheme.

2.2 Physical processes

To simulate the formation and evolution of stellar systems from gas, we introduce various physical processes into the GRAPE-SPH code; radiative cooling, star formation, feedback of SNe II, SNe Ia and SWs, and chemical enrichment including the mass dependence of SNe II. Here we describe the formulation and the assumptions of each physical processes.

2.2.1 *Radiative cooling*

Radiative cooling is modelled using an equilibrium cooling function. If gas is primordial with no heavy elements ([Fe/H] < -5), we compute the cooling rates using two-body processes of H and He, and free–free emission (Katz et al. 1996). These processes are collisional excitation of neutral hydrogen (H^0) and singly ionized helium (He^+), collisional ionization of H^0, He^0 and He^+, standard recombination of H^+, He^+ and He^{++}, dielectric recombination of He^+ and free–free emission. We compute a table, which lists $(\mathcal{H} - \Lambda)/n_H^2$ as a function of temperature and density. We then evaluate net cooling rates at intermediate values with cubic spline interpolation.

For metal-enriched gas ([Fe/H] $\geqslant -5$), we use a metallicity-dependent cooling function computed with the MAPPINGS III software by R.S. Sutherland (MAPPINGS III is the updated version of MAPPINGS II, which is described in Sutherland & Dopita 1993). The included processes are collisional line radiation, free–free and two-photon continuum, recombination, photoionization heating, collisional ionization and Compton heating. Heavy elements significantly enhance the cooling rate. At $T > 10^7$ K, Fe group line emission processes largely determine the cooling function, whereas at lower temperatures the lighter atoms such as C, O and Ne dominate. Although the metallicity effect is small at $T \sim 10^4$ K, the cooling rate with [Fe/H] $= 0$ is ~ 100 times larger than that for the primordial gas around $T \sim 10^5$ K. The radiative cooling, and hence the star formation rate (SFR), strongly depends on the metallicity. In the table of the cooling function that we use, cooling rates are given as functions of [Fe/H] and the elemental abundance ratios are set to be constant for given [Fe/H] according to the relations in the solar neighbourhood; Galactic halo stars (i.e. [O/Fe] $= 0.5$) for [Fe/H] $\leqslant -1$, and the solar values for [Fe/H] $\geqslant 0$, and interpolated the halo and solar values for $-1 <$ [Fe/H] < 0. Since the elemental abundance ratios depend on the star formation history and the inhomogeneous mixing of SNe II and Ia, the cooling tables depending on [O/Fe] are required to increase the accuracy.

2.2.2 *Star formation*

The treatment of star formation is similar to that in Katz (1992), which is widely used in GRAPE-SPH simulations. If a gas particle satisfies the following star formation criteria, a fractional part of the mass of the gas particle turns into a star particle. Since an individual star particle has a mass of 10^{-7} $M_\odot$, it does not represent a single star, but an association of many stars.

Our star formation criteria are (i) converging flow, (ii) rapid cooling and (iii) Jeans unstable on a particle scale;

$$\text{(i)} \quad (\nabla \cdot \boldsymbol{v})_i < 0, \tag{6}$$

$$\text{(ii)} \quad t_{\rm cool} < t_{\rm dyn}, \tag{7}$$

$$\text{(iii)} \quad t_{\rm dyn} < t_{\rm sound}. \tag{8}$$

where $t_{\rm cool}$, $t_{\rm dyn}$ and $t_{\rm sound}$ are the cooling time, the dynamical time of a particle and the sound crossing time, respectively, and are expressed as

$$t_{\rm cool} = \frac{\rho u}{\Lambda}, \tag{9}$$

$$t_{\rm dyn} = \frac{1}{\sqrt{4\pi G \rho}}, \tag{10}$$

$$t_{\rm sound} = \frac{h_i}{c_s}, \tag{11}$$

where μ is the mean molecular weight, u is the specific thermal energy, and c_s is the local sound speed.

We assume that the star formation time-scale is proportional to the dynamical time-scale;

$$t_{\rm sf} = \frac{1}{c} t_{\rm dyn}, \tag{12}$$

where the star formation parameter c is set to be 1.0. With $c = 0.1$, star formation takes place slowly, which results in too blue colours compared with the observation (this is discussed in greater detail in Section 4). The star formation rate is defined as

$$\frac{D\rho_*}{Dt} = -\frac{1}{t_{\rm sf}}\rho = -\frac{c}{t_{\rm dyn}}\rho = -c\sqrt{4\pi G}\rho^{3/2}, \tag{13}$$

where ρ_* is the stellar density. In other words, we adopt the Schmidt (1959) law, where the SFR is the power of the gas fraction and the power index is $n_s = 1.5$. This is consistent with the Hα observation of disc galaxies that implies $n_s = 1.3 \pm 0.3$ (Kennicutt 1989).

The star formation criteria are estimated with a time interval of $\Delta t_{\rm sf}$, which is set to be 2 Myr. The star formation probability P for a gas particle forming stars during Δt is given by Katz (1992) as

$$P = 1 - \exp\left(-\frac{c}{t_{\rm dyn}}\Delta t_{\rm sf}\right) = 1 - \exp(-c\sqrt{4\pi G\rho}\Delta t_{\rm sf}). \tag{14}$$

A random number between 0 and 1 is drawn to determine whether the gas particle forms stars during $\Delta t_{\rm sf}$: if P is larger than the random number, star formation occurs. P is larger for higher density, and the

typical density to form stars is higher with smaller c. For $c = 1.0$ and 0.1, most stars form in the region with $\rho \gtrsim 10^{-24}$ and 10^{-22} (g cm^{-3}), respectively. Practically, the lower limit of the gas density is given by c.

When the above criteria (equations 6, 7 and 14) are satisfied, a part of the material of the gas particle turns into a star particle, which newly forms near the gas particle. We follow the scheme in Nakasato & Nomoto (2003), where the initial mass of the star particle, m_*^0, is derived from the integration of the SFR over the time interval $\Delta t_{\rm sf}$;

$$m_*^0 = \rho \pi h_i^2 \left[1 - \exp\left(-\frac{c}{t_{\rm dyn}} \Delta t_{\rm sf}\right)\right]. \quad (15)$$

2.2.3 *Feedback*

The evolved stars eject surrounding materials and heavy elements via stellar winds and supernova explosions. These heat up, accelerate and enrich the circumstellar and interstellar medium. High-energy explosions such as supernovae produce high-temperature and low-density regions in the interstellar medium. In SPH methods, the numerical accuracy for high-density regions is much better than in mesh based methods, but the accuracy for low-density regions is poorer. In an SPH simulation such as those of Navarro & White (1993), the numerical resolution (100–1000 pc) is larger than the typical size of supernova remnants (several tens of pc). Thus, because of the nature of the SPH method and the lack of resolution in current computing resources, it is necessary to simplify the release of energy, momentum and mass from stars. We therefore assume that energy and heavy elements that are ejected from a star particle are equally distributed to the surrounding gas particles within a sphere of feedback radius $r_{\rm fb}$, which is a parameter that controls the mixing of heavy elements. We set $r_{\rm fb} = 1$ kpc, which gives a good fit to the chemical evolution in the Milky Way Galaxy (Kobayashi 2002).

In this paper, we distribute the feedback energy in purely thermal form. Navarro & White (1993) proposed that the energy produced by a supernova explosion is distributed to neighbour gas particles of the star particle mostly as a thermal energy and the rest is distributed as a velocity perturbation to the gas particles; the fraction of energy in kinetic form is given by a free parameter $f_{\rm kin}$. With $f_{\rm kin} > 0$, star formation efficiency is lower, surface brightness decreases at the centre and metal-rich gases blow out. If we adopt $f_{\rm kin} = 0.1$, the effective radius is too large and the metallicity gradient is too shallow (see Fig. 14 in Section 4).

The energy ejection rate $E_{\rm e}$ from a star particle as a function of age t is

$$E_{\rm e}(t) = m_*^0 \left[e_{\rm e,SW} \mathcal{R}_{\rm SW}(t) + e_{\rm e,II} \mathcal{R}_{\rm II}(t) + e_{\rm e,Ia} \mathcal{R}_{\rm Ia}(t)\right]. \quad (16)$$

$\mathcal{R}_{\rm SW}$, $\mathcal{R}_{\rm II}$ and $\mathcal{R}_{\rm Ia}$ are the rates of SWs, SNe II and SNe Ia, respectively, for which formulations are described in Section 2.2.4.

The energy of SWs from solar metallicity stars is estimated to be typically 0.2×10^{51} erg from the observation of OB associations (Abbott 1982). Although there should be a mass dependence where massive stars eject larger energies, we adopted the typical value because of a lack of observations. The chemical abundance of the star significantly affects SWs as $\dot{M} \propto Z^{0.68}$ (Leitherer, Robert & Drissen 1992), thus we include the metallicity effect for very massive stars;

$$e_{\rm e,SW} = \begin{cases} 0.2 \times 10^{51} \left(\dfrac{Z}{Z_\odot}\right)^{0.68} & (m_{2,\mu} < m \leqslant m_{\rm u}) \\ 0.2 \times 10^{51} & (m_{2,l} < m \leqslant m_{2,\mu}) \end{cases} \quad ({\rm erg}). \quad (17)$$

where Z is the metallicity of the star particle (see Section 2.2.4 for the upper- and lower-mass limits).

Since there are supernovae with 10 times larger energy than typical supernovae, hypernovae, the energy of all supernovae should not be the same. However, since the energy distribution function of supernovae has not been established, we adopt typical values of

$$e_{\rm e,II} = 1.4 \times 10^{51} (m_{2,l} < m \leqslant m_{2,\mu}) \, ({\rm erg}) \quad (18)$$

and

$$e_{\rm e,Ia} = 1.3 \times 10^{51} (m_{1{\rm a},l} < m \leqslant m_{1{\rm a},\mu}) ({\rm erg}) \quad (19)$$

for SNe II (Blinnikov et al. 2000) and SNe Ia (Nomoto, Thielemann & Yokoi 1984), respectively (see Section 2.2.4 for the upper- and lower-mass limits).

2.2.4 *Chemical enrichment*

A star particle is not a single star but an association of many stars. We assume that a star particle is, in fact, a simple stellar population, which is defined as a single generation of coeval and chemically homogeneous stars of various masses, i.e. it consists of a number of stars with various masses but the same age and metallicity. The mass, mass of heavy elements and the spectral energy distribution of the star particle evolve as massive stars die. From dying stars, gas is ejected into the interstellar medium by SWs, SNe II, and SNe Ia.

The mass of the stars associated with each star particle is distributed according to an initial mass function (IMF). The IMF is assumed to be invariant to time and metallicity as

$$\phi(m) \propto m^{-x}, \quad (20)$$

which is normalized to unity at $m_l \leqslant m \leqslant m_{\rm u}$. Theoretical arguments indicate that the IMF originates from fragmentation of a gas cloud almost independently of local physics in the gas (Low & Lynden-Bell 1976; Silk 1977). In the solar neighbourhood, the Salpeter IMF with $x = 1.35$ (Salpeter 1955) is a good approximation to the star counts and gives a good fit to many properties of disc galaxies (Kennicutt 1983). For ellipticals, the flatter IMF is favoured to explain the red colours of giant ellipticals (Kodama 1997). We then adopt $x = 1.10$ with the upper and lower masses of $m_l = 0.05$ and $m_{\rm u} = 120$ M$_\odot$.

The ejection rates of the mass and heavy element i ($E_{\rm m}$ and $E_{{\rm e},i}$) from the star particle are expressed as

$$E_{\rm m}(t) = m_*^0 \left[e_{\rm m,SW}(t) + e_{\rm m,II}(t) + e_{\rm m,Ia}(t)\right]. \quad (21)$$

and

$$E_{{\rm e},i}(t) = m_*^0 \left[e_{{\rm e},i,{\rm SW}}(t) + e_{{\rm e},i,{\rm II}}(t) + e_{{\rm e},i,{\rm Ia}}(t)\right]. \quad (22)$$

The ejection rates per mass are given by the following equations;

$$e_{\rm m,SW} = \left(\frac{Z}{Z_\odot}\right)^{0.68} \int_{\max[m_{l,\mu}, m]}^{m_\mu} (1 - w_m) \phi(m) \, {\rm d}m, \quad (23)$$

$$e_{\rm m,II} = \int_{m_l}^{m_{1,\mu}} (1 - w_m) \phi(m) \, {\rm d}m, \quad (24)$$

and

$$e_{\rm m,Ia} = m_{\rm CO} \mathcal{R}_{\rm Ia}(t). \quad (25)$$

Time dependence is in the lower-mass limit for integrals, the turn-off mass m_t, which is the mass of the star with the main-sequence (MS) lifetime $\tau_m = t$. For simplicity, the lifetime is determined as (David, Forman & Jones 1990)

$$\log \tau_m = 10.0 + (-3.42 + 0.88 \log m) \log m. \quad (26)$$

which gives a little (1.5 times) longer lifetime for $m \gtrsim 20\,M_\odot$ compared with the metallicity-dependent lifetime of Kodama & Arimoto (1997). In SWs and SNe II, stars eject the envelope materials outside the remnants. w_m is the remnant mass fraction, which is the mass fraction of a black hole, a neutron star or a white dwarf (WD), depending on the initial mass m. For SNe Ia, all of the evolved He core (i.e. C+O white dwarfs) is ejected, and the mass of the white dwarf at the SN Ia explosion is $m_{\rm CO} = 1.38\,M_\odot$.

Heavy elements are also ejected at the following rates;

$$e_{i,SW} = \left(\frac{Z}{Z_\odot}\right)^{0.8} \int_{\max[m_{\rm L,}, m_{\rm l}]}^{m_{\rm u}} (1 - w_m - p_{i,m,\rm II}) Z_i \phi(m)\,{\rm d}m, \tag{27}$$

$$e_{i,\rm II} = \int_{\max[m_{\rm L,}, m_{\rm l}]}^{m_{\rm L,u}} p_{i,m,\rm II}\phi(m){\rm d}m + \int_{\max[m_{\rm L,}, m_{\rm l}]}^{m_{\rm L,u}} (1 - w_m - p_{i,m,\rm II}) Z_i \phi(m)\,{\rm d}m, \tag{28}$$

and

$$e_{i,\rm Ia} = m_{\rm CO} p_{i,m,\rm Ia} \mathcal{R}_{\rm Ia}(t). \tag{29}$$

In SWs and SNe II, the heavy elements in the envelope are ejected. In SNe II and SNe Ia, explosive nucleosynthesis takes place and heavy elements are newly produced. $p_{i,m,\rm II}$ and $p_{i,m,\rm Ia}$ are the stellar yields, which are the mass fractions of newly produced and ejected heavy elements i and are derived from the supernovae nucleosynthesis model (Nomoto et al. 1997a,b) with $p_{i,m,\rm II} = 0$ for $m < 10\,M_\odot$. The upper and lower limits of SNe II are $m_{\rm 2,u} = 50\,M_\odot$ and $m_{\rm 2,l} = 8\,M_\odot$, respectively. For stars with 50–120 $M_\odot$, all the mass of an He core turns into a black hole. Although some metals such as carbon are produced in SWs, we neglect them here because their contribution is much smaller than that of supernovae. The dependence of $w_m, p_{i,m,\rm II}$ and $p_{i,m,\rm Ia}$ on the stellar metallicity has not been included.

The rates of SWs and SNe II, $\mathcal{R}_{\rm SW}$ and $\mathcal{R}_{\rm II}$, are obtained as

$$\mathcal{R}_{\rm SW} = \int_{\max[m_{\rm L,}, m_{\rm l}]}^{m_{\rm u}} \frac{1}{m}\phi(m){\rm d}m, \tag{30}$$

and

$$\mathcal{R}_{\rm II} = \int_{\max[m_{\rm L,}, m_{\rm l}]}^{m_{\rm L,u}} \frac{1}{m}\phi(m){\rm d}m. \tag{31}$$

For the SN Ia rate $\mathcal{R}_{\rm Ia}$, there are several alternative role debates. Here we adopt an SN Ia model based on the single degenerate scenario including metallicity effects (Kobayashi et al. 1998; Kobayashi, Tsujimoto & Nomoto 2000);

$$\mathcal{R}_{\rm Ia} = b \int_{\max[m_{\rm Ia,}, m_{\rm l}]}^{m_{\rm Ia,u}} \frac{1}{m}\phi(m){\rm d}m \int_{\max[m_{\rm d,}, m_{\rm l}]}^{m_{\rm d,u}} \frac{1}{m}\phi_{\rm d}(m)\,{\rm d}m. \tag{32}$$

The primary star is a C+O white dwarf formed from a stars with initial mass between $m_{\rm Ia,l} = 3\,M_\odot$ and $m_{\rm Ia,u} = 8\,M_\odot = m_{\rm 2,l}$. This SN Ia scenario has two types of secondary stars, main-sequence and red giant (RG) stars. We calculate the SN Ia rate for each binary system (i.e. the MS+WD and the RG+WD system) with respective b, $m_{\rm d,l}$ and $m_{\rm d,u}$, and combine them. The mass ranges of the companion stars are given by the simulation of binary evolution, and are 0.9–1.5 $M_\odot$ for the RG+WD system and 1.8–2.6 $M_\odot$ for the MS+WD system. Thus the lifetime of SNe Ia is ~2–20 and 0.5–1.5 Gyr, respectively. b is the binary parameter, which is the fraction of white dwarfs that eventually produce SNe Ia, and we adopt the same values, which are determined from the chemical evolution in the solar neighbourhood; $[b_{\rm RG}, b_{\rm MS}] = [0.02, 0.05]$ (Kobayashi et al. 2000).

The photometric evolution of a star particle is identical to the evolution of the simple stellar population, of which spectra are taken from Kodama & Arimoto (1997) as a function of age and metallicity. The absolute magnitude is calculated using passbands to the photometric system, which are the same as Kodama (1997).

2.3 Initial condition

A cosmological initial condition is generated with the following three steps. Throughout the paper, we set the cosmological parameters of $H_0 = 50\,{\rm km\,s^{-1}\,Mpc^{-1}}$, $\Omega_{\rm m} = 1.0$, $\Omega_\Lambda = 0$, and $\sigma_8 = 1.0$. (In the following, lengths and masses are for $H_0 = 50$.) First, we generate a periodic boundary condition with the lattice size 5 Mpc having a top-hat perturbation of amplitude 1σ or 3σ in radius 1.25 Mpc using the COSMICS package (Bertschinger 1995). This package uses the standard Zel'dovich approximation (Zel'dovich 1970; Efstathiou et al. 1985) to compute the displacements and velocities of the dark matter particles from a Gaussian random density field. The power spectrum of this density field represents the CDM spectrum for the above cosmological parameters. To generate a constrained density field, a path integral method is used (Bertschinger 1987). We set the parameters in COSMICS to obtain the density field realization with the desired number, mass and the starting redshift of $z \sim 25$. By changing the seed for the random number generator, we obtain a different density field. Giving the seed at random, we obtain a random sample of initial conditions.

Secondly, we pick up particles in a spherical region with the comoving radius of ~1.5 Mpc, the mass of $\sim 10^{12}\,M_\odot$ (baryon fraction of 0.1) and $N_{\rm tot}$ particles (the half for gas and the rest for dark matter). In this paper, we set two different resolutions; $N_{\rm tot} \sim 10\,000$ and 60 000. The mass of a dark matter particle is $\sim 1.8 \times 10^8$ and $\sim 3.0 \times 10^7\,M_\odot$, and the mass of a gas particle is $\sim 2.0 \times 10^7$ and $\sim 3.3 \times 10^6\,M_\odot$, respectively.

Thirdly, we give the initial angular momentum to the system in rigid rotation because the simulated field is not large enough to generate tidal torque. The typical spin parameter of a virialized halo in CDM cosmology ranges from 0.01 to 0.1 and the median is 0.05 according to the numerical simulations (e.g. Warren et al. 1992). We adopt a constant spin parameter λ as small as ~0.02. With larger λ, a spiral galaxy forms, if the galaxy does not undergo a major merger. If a major merger occurs, an elliptical galaxy forms even if the spin parameter is initially set to be as large as $\lambda \sim 0.1$. Thus, we should note that such ellipticals are not included in our sample. We also add the corresponding Hubble velocity to the velocity field of the sphere since the equation of motion is not integrated in comoving units but in physical units.

This scheme is similar to that in Katz (1992), and has been used in many works (e.g. Steinmetz & Müller 1994; Kawata & Gibson 2003; Nakasato & Nomoto 2003). Simulations from true CDM initial conditions excluding the artificial boundary effect were first carried out by Navarro & White (1994). We should bear in mind the boundary effect of our initial condition; materials in the outside of the simulated sphere are neglected, which makes the artificial cut-off of the mass accretion (this is discussed in greater detail in Section 4).

Table 1. Number of simulated galaxies.

	Run	Ellipticals	Dwarfs
High resolution ($N \sim 60\,000$)	13	18	0
Low resolution ($N \sim 10\,000$)	59	60	46
Total	72	78	46

3 RESULTS

3.1 Evolution histories

We simulate the chemodynamical evolution of 72 fields with different cosmological initial conditions (see Section 2.3). It takes $\sim$10 d to simulate one field with high resolution (the number of particles $N \sim 60\,000$) and 1 d with low-resolution ($N \sim 10\,000$). By the present time (i.e. $t = 13$ Gyr, $z = 0$), in 42 cases one galaxy forms in the centre of the field, in 16 cases one galaxy and several subgalaxies, and in 14 cases a few galaxies with comparable masses. We select galaxies that have stellar masses in a 20 kpc sphere larger than 4.5×10^7 $M_\odot$. Although many less-massive subgalaxies form, we discard them because our resolution is not high enough to study them in detail. We summarize the number of runs and the resulting galaxies in Table 1.

Fig. 1 shows the V-luminosity distributions in $\pm$10 kpc of 124 simulated galaxies. Luminosities are projected on the X–Y plane (the rotational axis is Z), and smoothed over 0.3 kpc. The number on the top of each image is the ID number in our simulation. The galaxies with the same number are in the same simulated field. The characters 'H' and 'L', respectively, denote the high- and low-resolution, and the following '1' and '3', respectively, denote the 1σ and 3σ overdense regions. The 18 galaxies in the left-hand side are obtained with high-resolution simulations, which clearly show triaxial distributions. The stellar masses span the range of $\sim 10^{9-11}$ $M_\odot$ and cD galaxies are not included in our sample. Among the 124 galaxies, 78 bright galaxies are elliptical galaxies, which have de Vaucouleurs' surface brightness profiles. Since the initial angular momentum is set to be small (spin parameter $\lambda \sim 0.02$), no spirals form. The remaining 46 faint galaxies are either dwarf ellipticals or dwarf irregular galaxies, all of which have small stellar masses as $M \lesssim 10^9$ $M_\odot$. Some dwarf galaxies show bright central cores, while others are diffusely distributing stellar systems.

Different galaxies undergo different evolution histories. The difference is seeded in the initial conditions. Galaxies form through the successive merging of subgalaxies with various masses, which varies between a major merger at one extreme and a monolithic

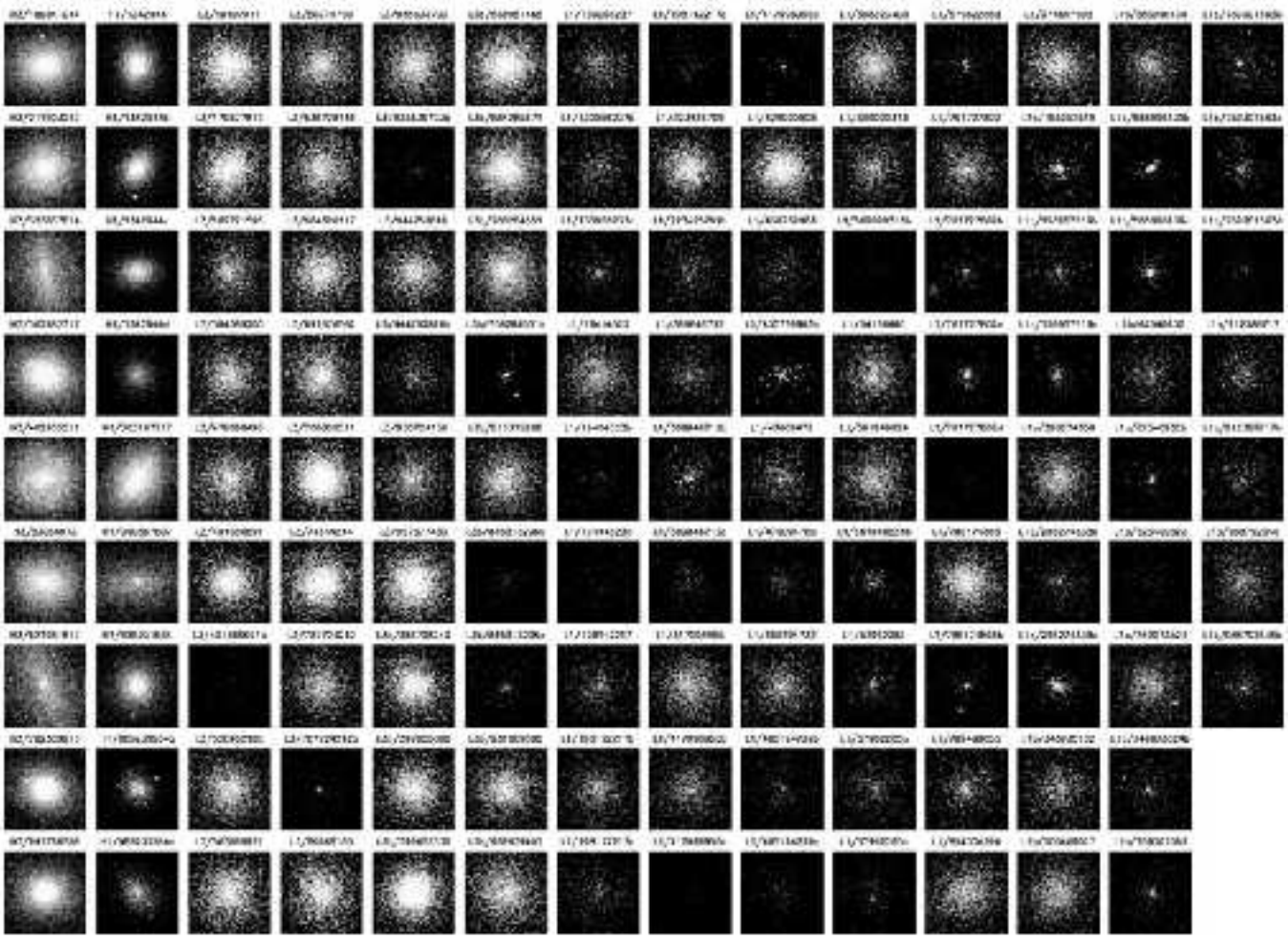

Figure 1. V-luminosity distributions in $\pm$ 10 kpc of 124 simulated galaxies with stellar masses of $\sim 10^{9-11}$ $M_\odot$. The number on the top of each image is the ID number in the simulation. This figure is available in colour in the on-line version of the journal on *Synergy*.

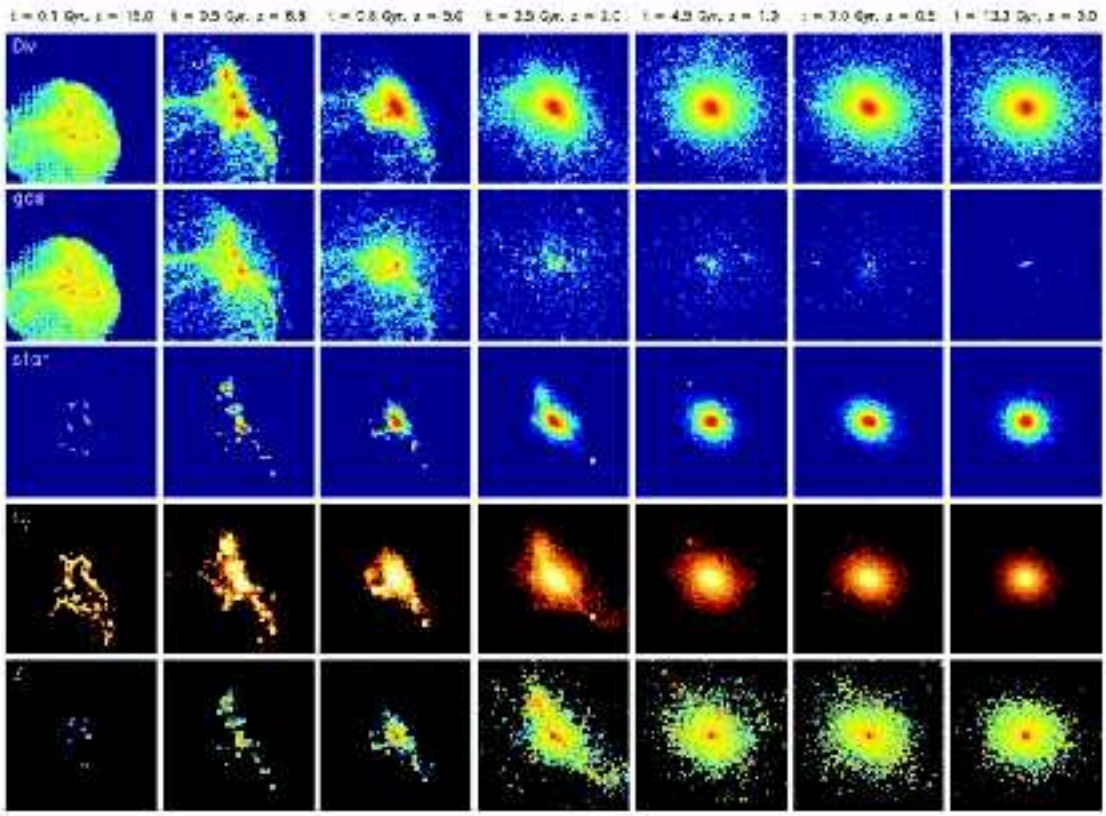

Figure 2. The evolutions in ±100 kpc of dark matter (first line), gas (second line), stars (third line), V-luminosity (forth line) and stellar metallicity (fifth line) of the galaxy that forms monolithically. The metallicity range is $\log Z/Z_{\odot} = -1$ to 0.4.

collapse of a slowly rotating gas cloud at the other. We show examples of the two cases from the high-resolution simulations in Figs 2 and 3, which show the evolution in ±100 kpc on the X–Z plane of dark matter (first line), gas (second line), stars (third line), V-luminosity (forth line) and luminosity weighted stellar metallicity (fifth line) of galaxies that form through monolithic collapse and through major merger, respectively.

Fig. 2 shows the evolution of a galaxy (ID H3/782389913) that forms monolithically. At the beginning, the system expands according to the Hubble flow. The CDM initial fluctuation produces the structures of nodes and filaments. Gas cores form in the nodes and stars form in the gas cores. The surface brightness is as high as 14 mag arcsec^{-2} in rest-frame V-band. Gas rich subgalaxies merge with one another and the protogalaxy coalesces at $z \gtrsim 3$. The accretion of small subgalaxies continues until $z \sim 2$, and after this no significant event happens. There is only a small amount of star formation at $z \lesssim 0.5$ and the luminosity of the galaxy decreases gradually toward $z = 0$.

Fig. 3 shows the evolution of a galaxy (ID H3/402905511) that undergoes a major merger at $z \simeq 2.0$. The primary galaxy forms in a large gas core at $z \gtrsim 3$. The secondary galaxy forms at the same time approximately 200 kpc away, which comes to the centre because of gravity and merges with the primary galaxy. The secondary initially passes through the primary ($z = 1.9$) and then oscillates decreasing in mass until the system is relaxed at $z = 0.9$. We should note that the edge of the dark matter distribution can be seen to fall on to the central object at $z \sim 6.8$ (Fig. 2) and 5.0 (Fig. 3). This means that the mass accretion after then may be underestimated.

We classify elliptical galaxies into the following five classes according to their merging histories.

(E1) *Monolithic*. Galaxies form through the assembly of many ($\gtrsim 10$) gas-rich subgalaxies with the stellar masses of $M \sim 10^9\,M_{\odot}$. Such assembly has generally finished by $z \sim 3$, by at least $z \sim 2$. The gas fractions [i.e. the mass ratio of gas to baryon $f_g \equiv M_g/(M + M_g)$] of merging galaxies are larger than 0.5. The material of subgalaxies quietly accretes on the central galaxy. It is difficult to discriminate these subgalaxies and this assembly looks like a monolithic collapse.

(E2) *Assembly*. Galaxies form through the assembly of subgalaxies with $M \sim 10^{10}\,M_{\odot}$. The gas fractions f_g of subgalaxies are as large as 0.4. Each subgalaxy has an evolved core, which violently merges with the others. While the subgalaxy passes through the central galaxy many times, many stars of the galaxy are stripped and some of them accrete on again.

(E3) *Minor merger*. The formation of the main component of the present-day galaxy is the same as the above two classes, but these galaxies undergo minor merger events at $z \lesssim 3$. We define the minor merger when the stellar mass ratio of the merging galaxies $f = M_2/M_1$ ($M_1 \geqslant M_2$) ranges from ~0.01 to ~0.2. With such minor merger events, the surface brightness profile and the metallicity gradients are not affected as much.

(E4) *Major merger*. Galaxies undergo the major merger with $f \gtrsim 0.2$ at $z \lesssim 3$. The mass of the primary galaxy is no more than five times larger than the mass of the secondary galaxy. The redshift $z \sim 3$ generally corresponds to the galaxy formation epoch and the main component of the present-day galaxy forms at $z \gtrsim 3$. Thus, the major merger occurs after most stars in the present-day galaxies formed. The merger event destroys the metallicity gradient that has existed in the pre-merger galaxy in a way depending on the mass ratio f and the gas mass of the secondary galaxy (see Section 3.3).

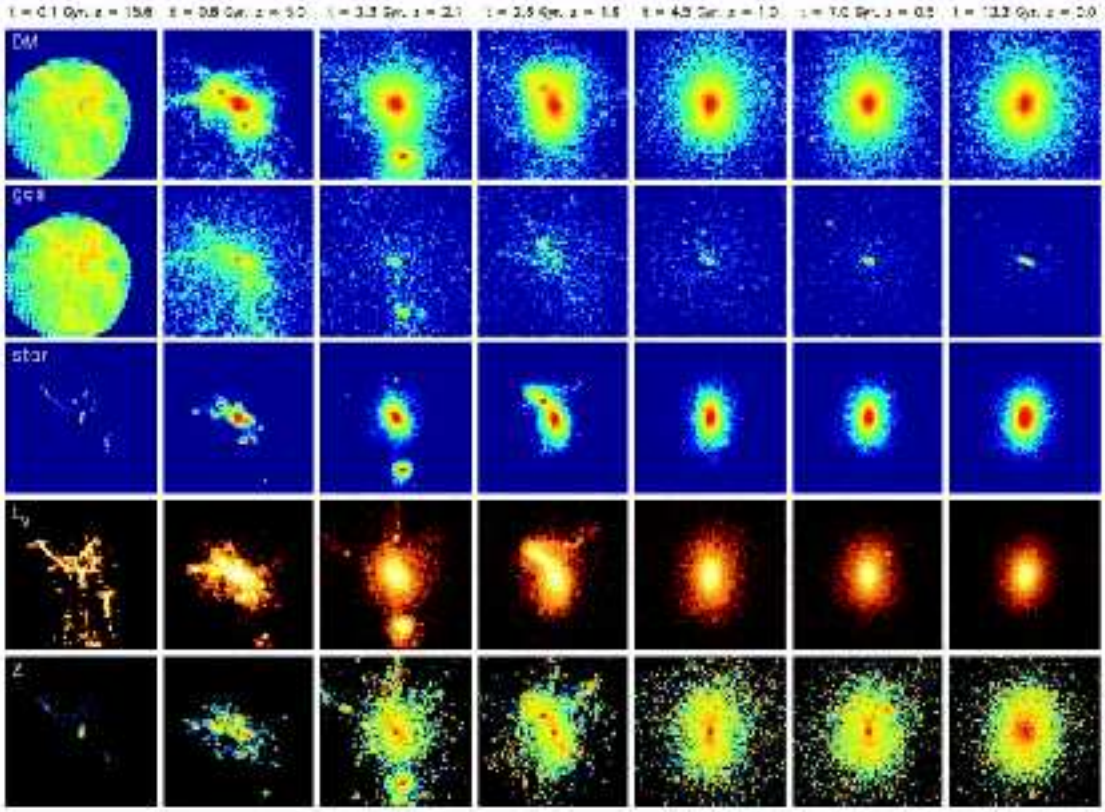

Figure 3. The same as in Fig. 2, but for a galaxy that undergoes a major merger at $z \simeq 2.0$.

(E5) *Multiple major mergers.* Galaxies undergo a major merger ($f \gtrsim 0.2$) and one or two other mergers with $f \gtrsim 0.1$.

Dwarf galaxies are classified into the following four classes according to their star formation histories. Observationally, the first class of galaxies are dwarf ellipticals, the others are dwarf irregulars.

(D1) *Initial starburst.* Galaxies form with the initial starburst at $z \gtrsim 1$. In some galaxies, many supernova explosions occur and cause the galactic winds. In other galaxies, the gas is not ejected completely, but the gas density is so small that only few stars form at lower redshifts. Thus the colours are red and these dwarfs follow the same colour–magnitude relation as giant ellipticals.

(D2) *Continuous star formation.* Galaxies grow though continuous star formation. After the initial starburst, there are the accretion of gas clumps and/or the interaction with other galaxies, which make the star formation continue to lower redshifts.

(D3) *Continuous star formation with recent starburst.* The same as (D2), but a starburst occurs at the recent 2–3 Gyr. Thus the galaxy colours are blue.

(D4) *Recent starburst.* Galaxies form through recent starbursts at $z \sim 0.7$. Such starbursts are induced by gas accretion and/or galaxy interactions. The colours are blue, and it is impossible to distinguish (D3) and (D4) with colours alone.

The number of galaxies in each class is (i) 5 (4.0 per cent), (ii) 18 (15 per cent), (iii) 19 (15 per cent), (iv) 25 (20 per cent), (v) 11 (8.9 per cent), (D1) 20 (16 per cent), (D2) 13 (10 per cent), (D3) 9 (7.3 per cent) and (D4) 4 (3.2 per cent). The percentages of non-major merger (E1–3) and major merger galaxies (E4, 5) are 34 and 29 per cent, respectively. We should note that the number of merger galaxies tends to be underestimated because of the boundary effect of our initial condition.

Fig. 4 shows the star formation rates [log SFR ($M_\odot$ yr^{-1})] as a function of time t (Gyr), which are derived from the ages and masses of stars that belong to the galaxy at present. Thus, these rates are not for stars formed in the region that is defined as the galaxy at each redshift, but for stars that formed anywhere and are today part of the galaxy. This definition of the SFR will be the same as in any observation that estimates the star formation history of a galaxy from its stellar populations. As is clearly shown, all elliptical galaxies form with an initial starburst at $z \gtrsim 2$, whereas dwarf galaxies undergo relatively continuous star formation. The SFR decreases because the gas is exhausted in the galaxy. The secondary starburst is induced by the accretion of gas clumps and/or the merging of gas-rich galaxies. Not all merging events induce a secondary starburst; the fraction of merging events that induce such a starburst is approximately 10 per cent. For all ellipticals, the initial starburst is always larger than the secondary one. The typical time-scale of the initial starburst is found to be 1–2 Gyr, which is much longer than the 0.1 Gyr that is commonly adopted in the one-zone model (e.g. Koduma & Arimoto 1997). Such an SFR is due to the artificial cut-off of mass accretion caused by our initial condition, but is required from the observation of ellipticals as summarized in Section 1.

We should note that star formation has not completely stopped at present in most elliptical galaxies. Galactic winds are hard to generate in our simulated giant ellipticals (this is discussed in greater detail in Section 4). At the centre of the present-day galaxy, the dynamical potential is so deep that the gas density is high. In such regions, super metal-rich stars ($Z \sim 10\,Z_\odot$) form in the simulation. In several dwarf galaxies with $M \lesssim 10^9\,M_\odot$ (e.g. ID L1/223425799b and L1/430769963), weak galactic winds can be seen even if $f_{\rm bin} = 0$.

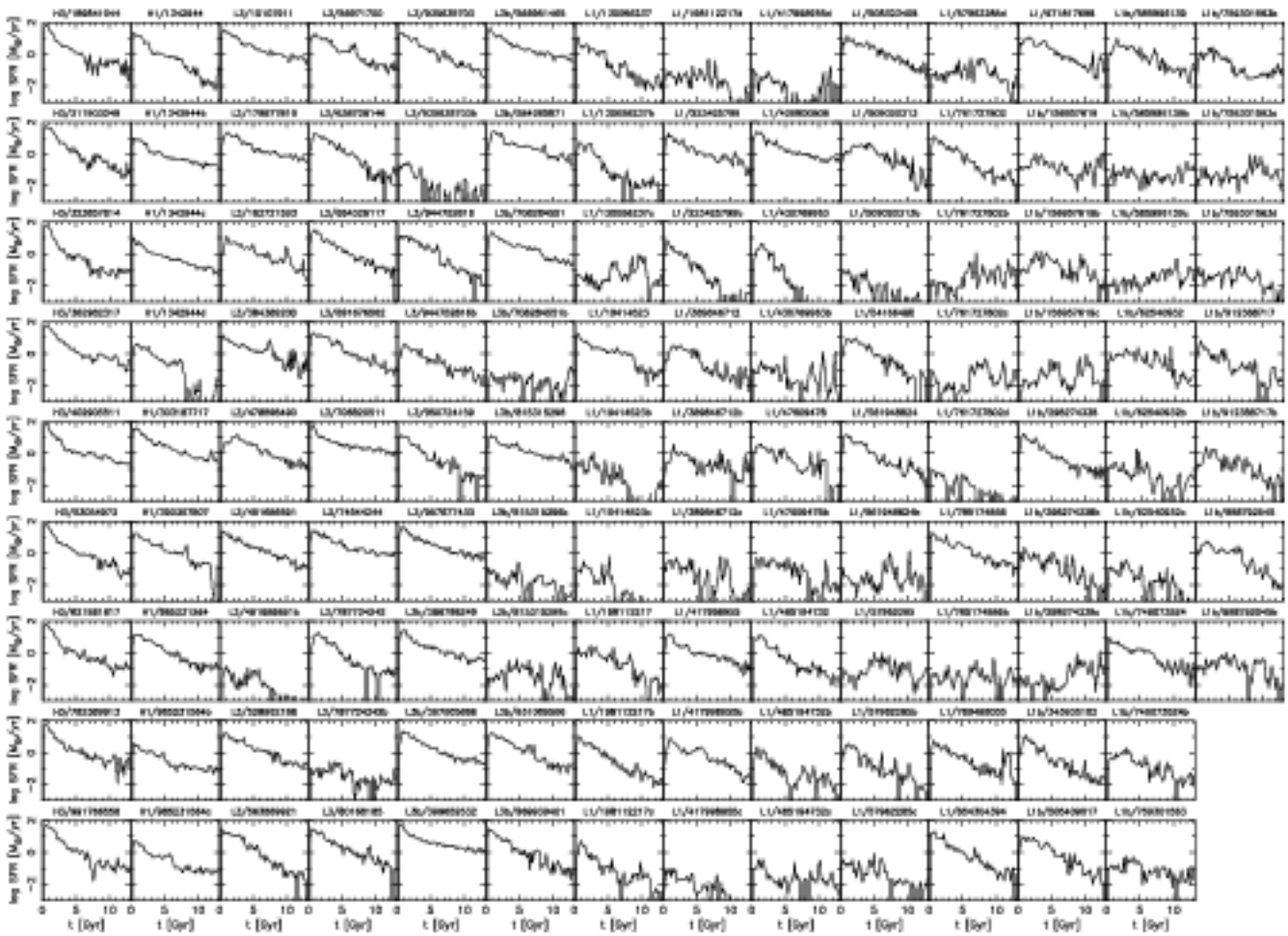

Figure 4. The star formation rates [log SFR ($M_\odot$ yr^{-1})] as functions of time t (Gyr) in a present-day galaxies ($r \leqslant 20$ and $|Z| \leqslant 100$ kpc).

However, enough gas is heated up and blows away gradually by the input of the thermal energy of supernovae. The global gas fraction of the simulated fields spans over 50–90 per cent, and the gas fraction in a galaxy (a sphere of $2r_e$) is 1–10 and 30–80 per cent for giants and dwarfs, respectively. The fraction of heavy elements locked into stars in a galaxy spans 20–40 per cent which is consistent with the observation (e.g. Renzini 2002).

3.2 Metallicity gradients

Galaxies are observed in projection on the sky. In order to compare the simulated results with observation, foreground and background particles should be excluded properly. We define a galaxy as the projection of $|Z| \leqslant 100$ kpc on the X–Y plane. Below radius r means a projected radius. We then derive the effective radius r_e by fitting a de Vaucouleurs' law to the surface brightness profile. For the simulated galaxies, we exclude the central region with $r = 0$–1 and 0–2 kpc when fitting simulations with high- and low-resolution, respectively, because the surface brightness is smeared out due to the softening of the gravity. In the outer region, to derive proper effective radii in the simulation, we use large enough regions such as 40–80 kpc. In the case where galaxies show a local excess in the surface brightness because of the existence of the satellite subgalaxies, we only use the inner part.

Observationally, metallicity gradients are derived from the line-strength gradients, and line-strength is converted to metallicity using an index–metallicity relation derived from spectral synthesis models (e.g. Kodama & Arimoto 1997). Thus the observed metallicity is the luminosity weighted metallicity. In the observational data, the gradients are smeared out due to poor seeing conditions at galaxy centres with $\log r/r_e \lesssim -1.5$, and in the outer regions with $\gtrsim 2r_e$ errors arising from the sky subtraction give poor fits. Kobayashi & Arimoto (1999) excluded these regions from the fitting. In the simulation, we provide the metallicity weighted by V-luminosity, because the absorption indices usually observed such as Mg_2 and Fe_1 are in the V-band. Since we find no significant difference in the metallicity gradients at $r = 1$–2 kpc for the high- and low-resolutions, the innermost boundary of the fitting region is set at 1 kpc for both resolutions. This value is larger than the radius of $\log r/r_e \sim -1.5$. The outer boundary is set at $2r_e$ for most galaxies and at 10 kpc for galaxies in the case with small r_e. The contribution of satellite galaxies is also excluded.

Fig. 5 shows the metallicity gradients of 124 galaxies, where [M/H] is plotted against $\log r/r_e$. The thick and thin lines show the oxygen and iron abundance gradient, respectively. The fitting lines are shown with dotted lines. The dotted vertical lines show the maximum radii used in the fitting. As is clearly seen, the metallicity gradients are various, some are steep and others flat.

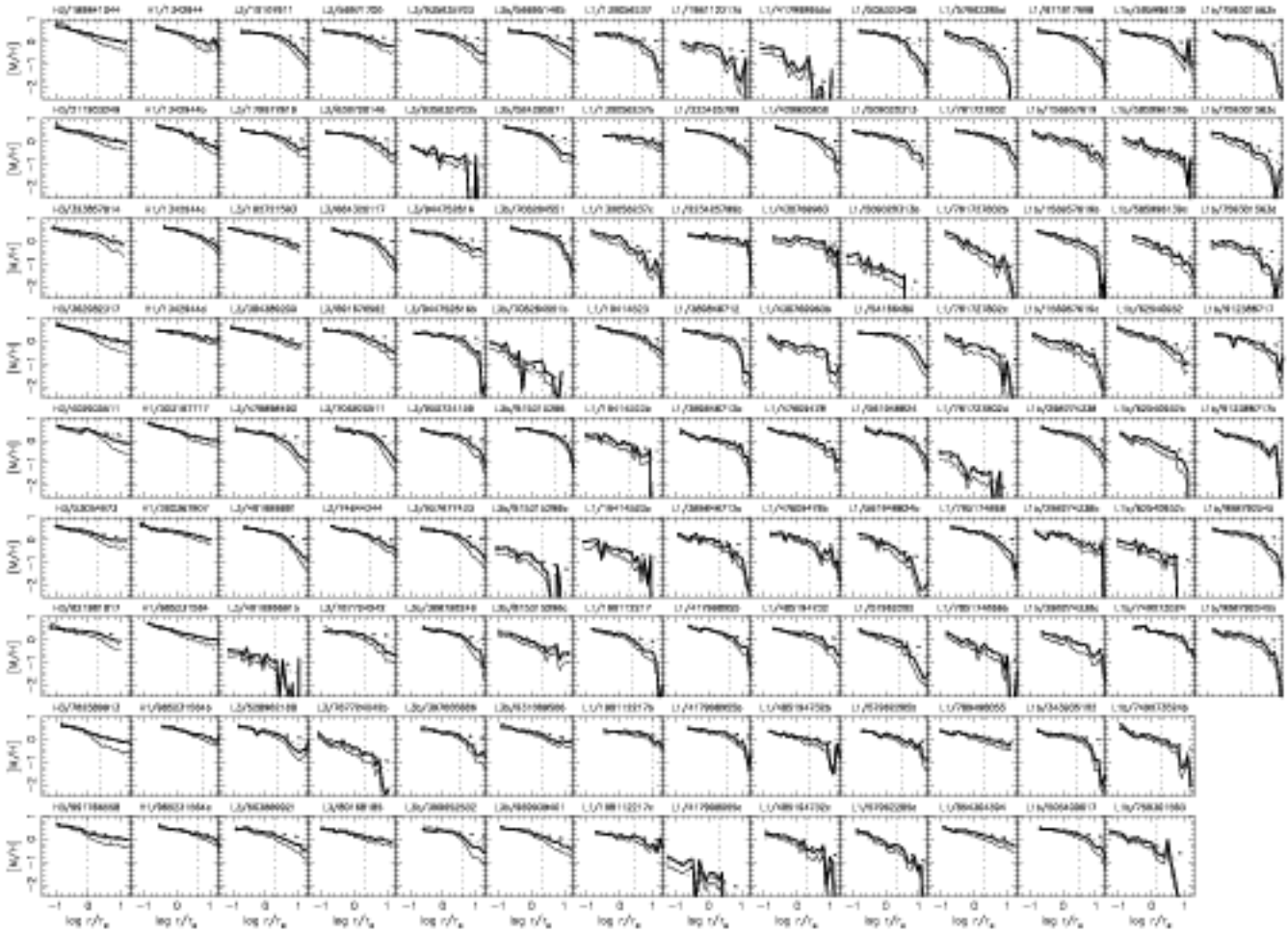

Figure 5. The metallicity gradients, where [M/H] is plotted against $\log r/r_e$. The thick and thin lines show the oxygen and the iron abundance gradients, respectively. The fitting lines are shown by dotted lines. The dotted vertical lines show the maximum radii used in the fitting.

3.3 Relation versus mass?

Fig. 6 shows the V-luminosity weighted metallicity gradients versus stellar mass within r_e (a and d), total luminosities derived from the de Vaucouleurs' law (b and e) and luminosity weighted mean stellar metallicities in r_e (c and f). The upper (a–c) and lower panels (d–f) show the gradients of oxygen and iron abundances, respectively. All points are for the simulated galaxies and the large points denote galaxies simulated with high resolution. The symbols show the merging histories for elliptical galaxies and star formation histories for dwarf galaxies: (E1) monolithic (filled circles), (E2) assembly (filled squares), (E3) minor merger (filled triangles), (E4) major merger (open squares) and (E5) multiple major merger (open circles); (D1) initial starburst (asterisks), (D2) continuous star formation (crosses), (D3) continuous star formation with recent starburst (plus), and (D4) recent starburst (three-pointed stars).

The remarkable result is that there is no correlation between the gradients and masses or luminosities in Fig. 6. The lack of these relations has already been found in the observational data and the origin of the scatter has been debated (Kobayashi & Arimoto 1999). It seems that more metal-rich simulated ellipticals tend to have steeper gradients, but it is hard to find any relation if simulated dwarfs are included. The origin of scatter is clearly shown with the symbols; the galaxies that form monolithically (filled circles and squares) have steeper gradients and the galaxies that undergo major mergers (open circles and squares) have shallower gradients. Therefore, we conclude that the metallicity gradients do not depend on the galaxy mass and the variety of the gradients stems from the difference in the merging history.

The distributions of metallicity gradients for (E1) monolithic collapse, (E2) assembly and (E3) minor merger are very similar. The minor mergers do not affect the metallicity gradients as much. The distributions for (E4) major merger and (E5) multiple major mergers are also similar. Then we combine the five classes into two large classes: (A) non-major merger galaxies including (E1–3) and (B) major merger galaxies including (E4, 5). Fig. 7 shows the histograms of the metallicity gradients (∇_V) for the two classes using metallicity Z (top panel), oxygen (middle panel) and iron abundance (bottom panel). The distributions for (A) non-major merger (grey area) and (B) major merger (hatched area) galaxies are different. The typical gradients for non-major merger and major merger galaxies are $\Delta\log Z/\Delta\log r \simeq -0.30$ and -0.22, Δ[O/H]$/\Delta\log r \simeq -0.30$ and -0.18, and Δ[Fe/H]$/\Delta\log r \simeq -0.45$ and -0.38, respectively. The galaxies with gradients as steep as $\Delta\log Z/\Delta\log r \leqslant -0.35$ are all non-major merger galaxies.

The thick lines show the observed metallicity gradient distributions for Mg$_2$ (top and middle panels) and Fe$_1$ (bottom panel) using data from Kobayashi & Arimoto (1999). (The reason for comparing

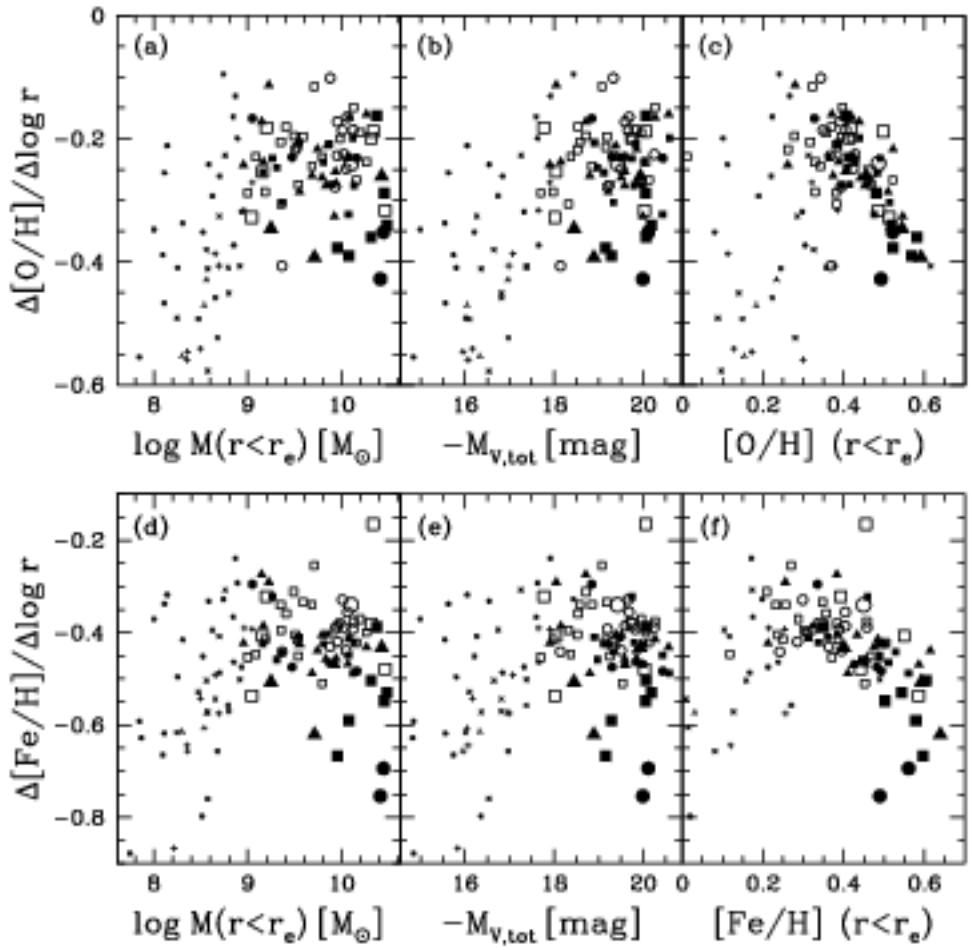

Figure 6. Metallicity gradients versus (a), (d) stellar masses in r_e, (b), (e) total luminosities and (c), (f) mean stellar metallicities in r_e. The upper (a)–(c) and lower panels (d)–(f) show the gradients of oxygen and iron abundances, respectively. All points are for the simulated galaxies and the large points denote galaxies simulated with high resolution. The symbols that show the merging histories for elliptical galaxies and star formation histories for dwarf galaxies are: (E1) monolithic (filled circles), (E2) assembly (filled squares), (E3) minor merger (filled triangles), (E4) major merger (open squares) and (E5) multiple major merger (open circles); (D1) initial starburst (asterisks), (D2) continuous star formation (crosses), (D3) continuous star formation with recent starburst (plus) and (D4) recent starburst (three-pointed stars).

oxygen gradients with the Mg_2 observation is that the yields relative to solar value are almost the same between O and Mg.) The simulated Z gradients are consistent with the Mg_2 observation both with the mean value of $\Delta\log Z/\Delta\log r \simeq -0.3$ and the dispersion of ± 0.2. The oxygen gradients are shallower by 0.05 dex than the Mg_2 observation. This is because the Mg_2 index is not a good indicator for magnesium abundance, but rather for metallicity (Tripicco & Bell 1995; Kobayashi & Arimoto 1999). For iron, the simulated Fe gradients are steeper than the observation, even if one takes into account the much larger observational errors of Fe_1 than Mg_2. This is because in the simulation the star formation does not completely terminate in the galaxy centre (see Section 4).

From the observed metallicity gradients, we can estimate the fraction non-major merger and major merger galaxies. Using the Mg_2 observation, we derive the numbers of nearby elliptical galaxies with steep gradients of $\Delta\log Z/\Delta\log r \leqslant -0.3$ and flat gradients of > -0.3 as 25 and 21, respectively. If we take alternative threshold value of $\Delta\log Z/\Delta\log r = -0.25$, the numbers become 30 and 16, respectively. Therefore, the fraction of non-major merger galaxies is half or two third. Even if we take account of some problems involved in our initial condition (see Section 4 for further details), there exist non-major merger galaxies and major merger galaxies half and half. The observed variation in the metallicity gradients cannot be explained by either the *monolithic collapse* only or the *major merger* only. It is well reproduced in the present model where both formation processes arise under the CDM scheme.

3.4 Evolution of gradients via mergers

The spatial distribution of metallicity is already shown in the last line of Figs 2 [(E1) the monolithic case] and 3 [(E4) the major merger case]. The metallicity is enhanced in the high-density region and radial metallicity gradients appear in protogalaxies at $z \sim 5$. After the major merger at $z \simeq 2.0$, many metal-rich stars move to the outer region of the galaxy. In the monolithic case, the metal-rich region is concentrated, while in the major merger case the metal-rich region extends over ± 10 kpc. The present metallicity gradients are $\Delta\log Z/Z_\odot\,/\Delta\log r = -0.46$ and -0.19, respectively.

Figs 8 and 9 show the time evolutions of metallicity gradients for (E1) the monolithic case and (E5) the multiple major merger case, respectively. The thick and thin lines are for the oxygen and iron abundances, respectively. The solid and dotted lines indicate

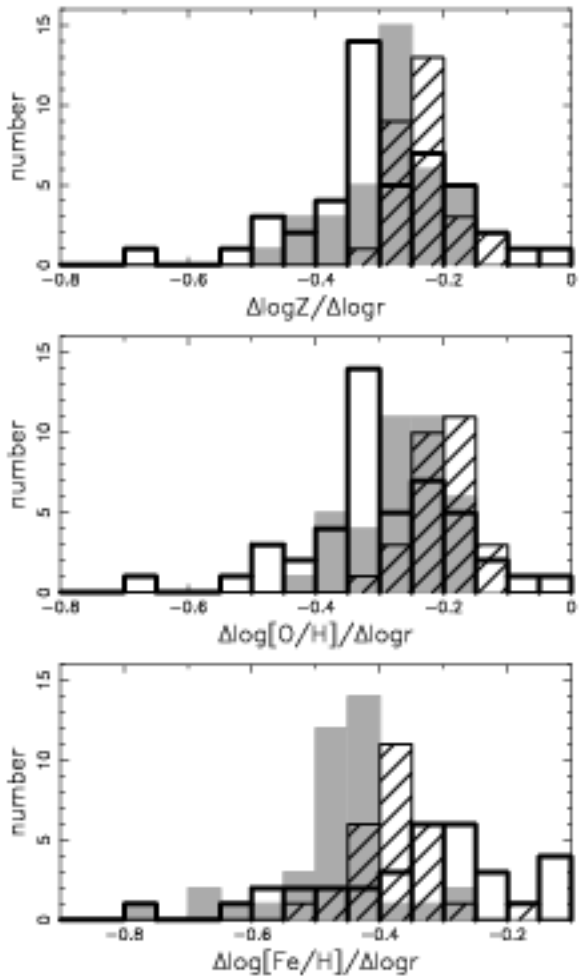

Figure 7. The histograms of the gradients for metallicity Z (upper panel), oxygen (middle panel) and iron abundance (lower panel). The grey and hatched areas are for non-major merger and major merger galaxies, respectively. The thick lines show the observation with Mg_2 (upper and middle panels) or Fe_1 (lower panel) index from Kobayashi & Arimoto (1999).

the gradients weighted by V-luminosity and mass, respectively. The gradients are underestimated if the metallicity is weighted by mass.

Fig. 8 shows the gradient evolution of ID H3/782389913. This galaxy forms through the assembly of three galaxies with the stellar masses of 8×10^9, 4×10^9 and 4×10^9 $M_\odot$, and thus the initial gradient is not so steep, Δ[Fe/H]/$\Delta \log r \simeq -0.9$. This assembly had finished by $z \simeq 3.7$ ($t \simeq 1.2$ Gyr). Then the galaxy evolves quietly and the metallicity gradient is kept nearly constant. At $z \simeq 0.1$ ($t \simeq 10$ Gyr), a small galaxy with $\sim 10^{10}$ $M_\odot$ accretes. The small star formation is induced, which changes the gradient by 0.1 dex temporarily.

Fig. 9 shows the gradient evolution of ID H3/3903678O7. This galaxy undergoes the major mergers three times at $z \simeq 1.3$, 0.9 and 0.5 ($t \simeq 3.7$, 5.1 and 6.9 Gyr). The mass ratios are $f = 0.47$, 0.16 and 0.24, respectively. The initial starburst produces the metallicity gradient of Δ[Fe/H]/$\Delta \log r \sim -1.2$. The major merger event is so violent that the gradient decreases by 0.7 dex to Δ[Fe/H]/$\Delta \log r \simeq -0.5$. The second and third merger events are not so active, and the gradient becomes Δ[Fe/H]/$\Delta \log r \simeq -0.4$ and -0.3 at the end of the merger event, respectively.

The initial gradient is determined during the initial starburst at $z \gtrsim 3$. The gradient is steeper in the case of quiescent gas accretion

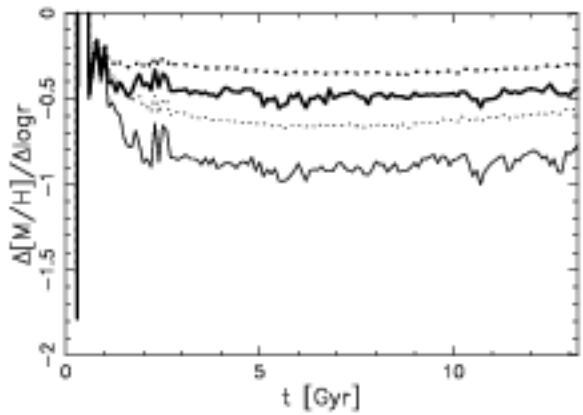

Figure 8. The evolution of metallicity gradients for the monolithic collapse case. The thick and thin lines are for the oxygen and the iron abundances, respectively. The solid and dotted lines are the gradients weighted by V-luminosities and masses, respectively.

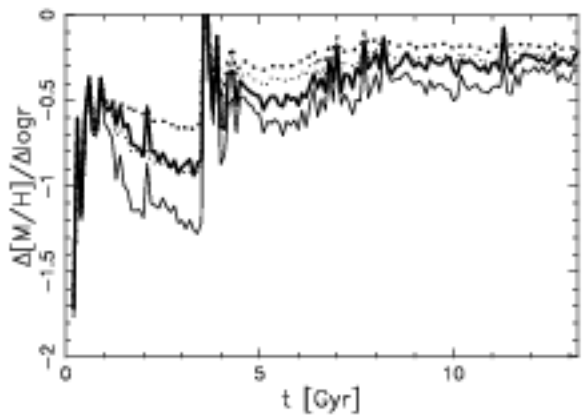

Figure 9. The same as in Fig. 8, but for the major merger case. Mergers takes place at $t \simeq 3.7$, 5.1 and 6.9 Gyr.

and is shallower in the case of violent assembly of subgalaxies. As a result, the initial gradients span from Δ[Fe/H]/$\Delta \log r \simeq -1.5$ to -1.0. Since the gradients evolve a great deal after this time, the initial gradients cannot be inferred from the present gradients.

The metallicity gradients definitely become shallower when galaxies merge. However, the formation and destruction of gradients via mergers are complicated. To find out some rules, we examine the physical conditions at the 151 merging events that occur in our simulations of giant galaxies. Fig. 10 shows (a) mass ratios $f = M_2/M_1$ ($M_1 \geqslant M_2$), (b) ratios of gas mass $M_{g,2}/M_{g,1}$, (c) gas fractions of primary galaxies $f_{g,1}$, and (d) those of secondary galaxies $f_{g,2}$ against redshifts z. The averages of f and $f_{g,1}$ in each redshift bin decrease toward $z = 0$ because the stellar masses of primary galaxies increase. The average of $M_{g,2}/M_{g,1}$ is larger than that of f, and is constant at ~ 0.5. $f_{g,2}$ is larger than $f_{g,1}$, and spans from 0 to 1. This is because star formation strongly depends on gas density and takes place slowly in the less-massive secondary galaxies. At $z < 1$, some major mergers ($f \gtrsim 0.2$) have $M_{g,2}/M_{g,1} \gtrsim 0.5$, which means that the secondary galaxies have comparable mass and gas content to the primaries. These induce strong star formation (surrounded by circles). Relatively weaker star formation (surrounded by triangles) is induced by mergers with $f_{g,2} \gtrsim 0.5$, which means that the stellar mass of the secondary is small and the secondary galaxy behave like a gas cloud.

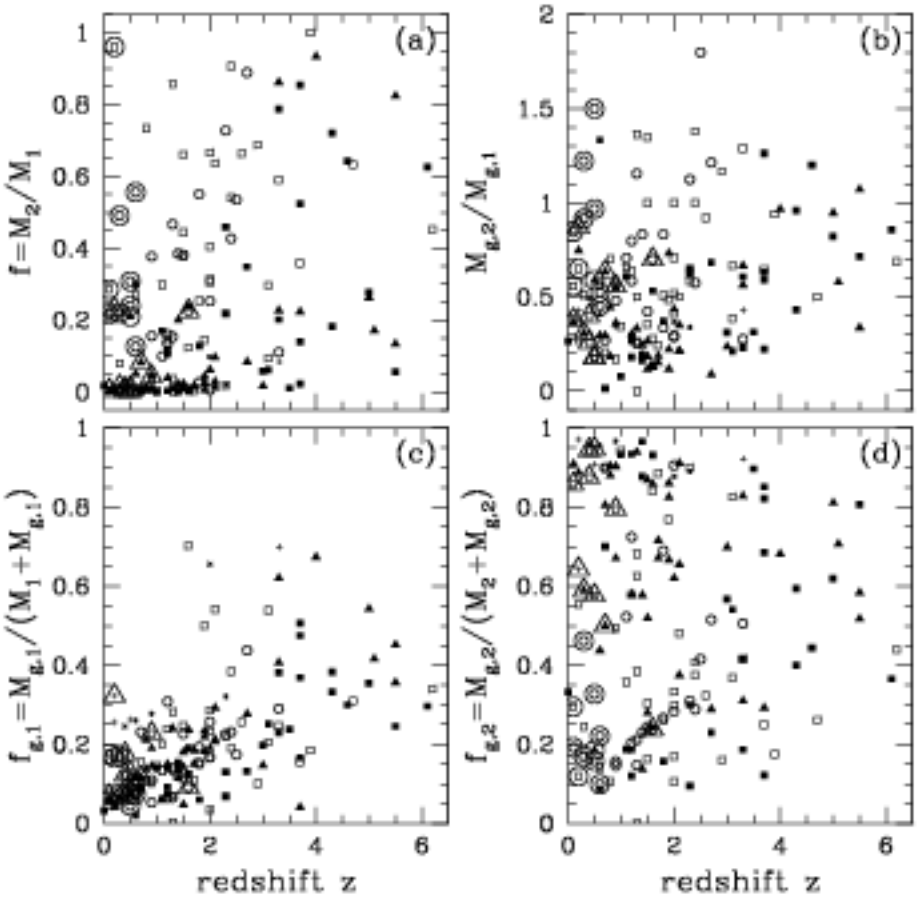

Figure 10. (a) Mass ratios $f = M_2/M_1$ ($M_1 \geqslant M_2$), (b) ratios of gas mass $M_{g,2}/M_{g,1}$ and (c), (d) gas fractions ($f_{g,1}$ and $f_{g,2}$) of the primary and secondary galaxies versus redshifts z. The symbols are the same as in Fig. 6. The points surrounded by large circles/triangles indicate that strong/moderate star formation is induced.

Fig. 11 shows the change of gradient, $\Delta(\Delta[\mathrm{Fe/H}]/\Delta\log\ r)$, caused by a merging event at $z < 3$ against various physical conditions: (a) f, (b) $M_{g,2}/M_{g,1}$, (c) $f_{g,1}$, (d) and $f_{g,2}$. The gradient change strongly depends on the mass ratio f. The mergers with $f > 0.2$ decrease the gradients by at least 0.5 dex. This is the reason why we have defined major mergers as those with $f > 0.2$. A major merger changes the orbits of stars. The stars that are in the centre and have high metallicities are able to move to the outer region of the galaxy. However, if the secondary galaxy contains as much gas as the primary galaxy (i.e. $M_{g,2}/M_{g,1} \gtrsim 0.5$) and strong star formation is induced (surrounded by circles), then the gradient change stays smaller than 0.5 dex. This is because such star formation takes place after the gas falls into the centre of the primary galaxy and increases the metallicity at the centre, resulting in a small gradient change. Sometimes the merging of a gas rich galaxy ($f_{g,2} \gtrsim 0.5$) also induces moderate star formation (surrounded by triangles). In this case, star formation takes place in the outer region of the galaxy and the gradient change can be as large as $\sim$0.5 dex, even if $f \sim 0$. In some cases without a merging event, a similar star formation is induced by late gas accretion and the metallicity gradient gradually becomes shallower.

By showing a similar figure in van Albada (1982), we argue that dynamical information on the orbits of N-body particles is not fully wiped out by a merger, but fairly lost to the change in the metallicity gradient. Figs 12 and 13 show the energies $E = v^2/2 + \Phi$ of particles before and after a merging event. Large E means that a particle has an extended orbit. Fig. 13 shows the energies at 3.5 and 4.9 Gyr for the first major merger at $\simeq$3.7 Gyr of the galaxy ID H3/390367807 that undergoes a triple major merger (see Fig. 9 for the gradient evolution). Fig. 12 shows the same but for the non-merger galaxy ID H3/782389913. Clearly, the dispersion for the merger galaxy is much larger than the non-merger galaxy.

In summary, whether the merging event changes the metallicity gradient is mainly influenced by two factors: (i) the mass ratio of the merging galaxies f and (ii) the induced star formation. The evolution of the gradients via merging events is based on the following three processes. (i) Destruction by mergers to an extent dependent on f. (ii) Regeneration due to the central star formation induced at a rate dependent on $M_{g,2}/M_{g,1}$. (iii) Passive evolution as star formation is induced in the outer regions at a rate dependent on $f_{g,2}$. We note that the gradient change is underestimated if the metallicity is not weighted by luminosity as in the observation, but by mass as in previous simulations.

4 DISCUSSION

The global properties of elliptical galaxies depend mainly on their masses, while their metallicity gradients are greatly affected by their merging history. Merging histories can thus, in principle, be inferred from the observed metallicity gradients of present-day galaxies. The dispersion in metallicity gradients for galaxies with similar merging histories is not small (Fig. 7) and so it may be difficult to determine

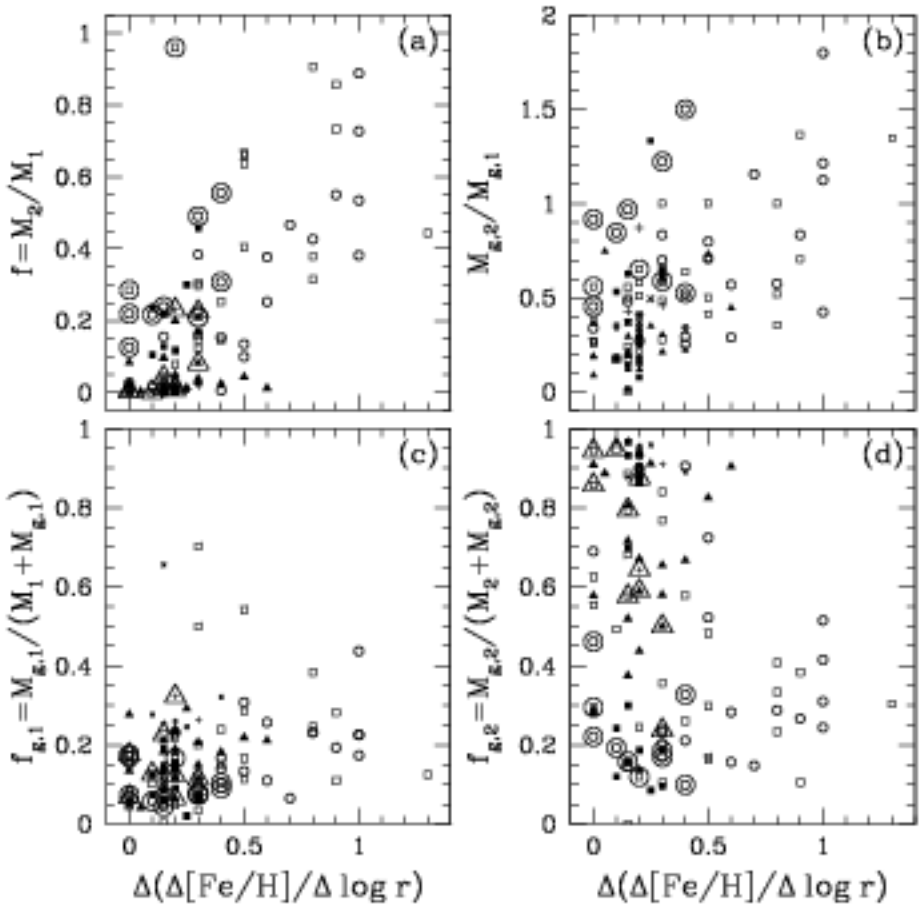

Figure 11. The gradient change $\Delta(\Delta[\mathrm{Fe/H}]/\Delta \log r)$ before and after the merging event at $z < 3$ versus (a) mass ratios f, (b) ratios of gas mass $M_{g,2}/M_{g,1}$ and (c), (d) gas fractions ($f_{g,1}$ and $f_{g,2}$). The symbols are the same as in Fig. 6. The points surrounded by huge circles/triangles indicate that strong/moderate star formation is induced.

the merging history of an individual galaxy from its metallicity gradient. However, it should be possible to estimate the fractions of non-merger and merger galaxies using the statistics of metallicity gradients. For example, if the fractions are estimated for field and cluster galaxies, it should provide information concerning environmental effects on galaxy formation. Even allowing for the uncertainties in available observations of nearby galaxies, our predicted difference between gradients of non-merger and merger galaxies is large enough to be detected.

We should note that there are two problems in the simulated galaxies, which cannot be improved by changing the parameters in the present model. One is that galactic winds do not occur in large galaxies in the simulations and star formation never terminates completely. The colours of our galaxies thus tend to be bluer than the observation and the $B-V$ colour distribution extends to 0.4-mag bluer. In our galaxy centres, the colour gradients tend to have the opposite slope to the metallicity gradients, because the stellar populations there are young. Such late star formation takes place in the central 1 kpc and this region is carefully excluded when estimating metallicity gradients in this paper. This problem arises from the SPH method and the feedback scheme. If we include the kinetic feedback with $f_{\rm kin} > 0$, surface brightness decreases at the centre and metal-rich gases blow out. However, these result in too large effective radii and too shallow metallicity gradients to meet the observation. Fig. 14 shows the surface brightness profiles and metallicity gradients with (dash-dotted line) and without (solid line) $f_{\rm kin}$ using the same initial condition. With $f_{\rm kin} = 0.1$, the surface brightness decreases by $\sim$2 mag at the centre, which results in $r_{\rm e} = 8.1$ kpc ($r_{\rm e} = 4.3$ kpc for $f_{\rm kin} = 0$). The metallicity gradient is almost flat within $r_{\rm e}$. To describe galactic winds with the kinetic feedback, the star formation scheme should be modified simultaneously.

We note that our predictions for oxygen abundance are not changed as much, whereas the iron abundance should decrease especially at the galaxy centre. In Fig. 6, there appears to be a relation between the iron abundance and the iron gradients. This is because late star formation at the galaxy centre increases the iron abundance and steepens the iron gradients at the same time. Such a relation can disappear if the galaxy model is improved. In Fig. 7, the mean value of simulated iron gradients is steeper than observed. This is also caused by the same reason. If the galaxy model is improved so as to cause a galactic wind to blow, iron gradients for non-merger galaxies will become similar to their oxygen gradients. However, iron gradients for merger galaxies will be still steeper than the oxygen gradients. The difference between iron and oxygen gradients, i.e. [O/Fe] gradients, may be the best indicator of the formation history of the galaxy. To discuss [O/Fe], observational data of a high enough signal-to-noise ratio is required and the spectral population synthesis models should be prepared for various [O/Fe].

The other problem is that simulated galaxies are more extended, and thus there is an offset in the radius–magnitude relation. This

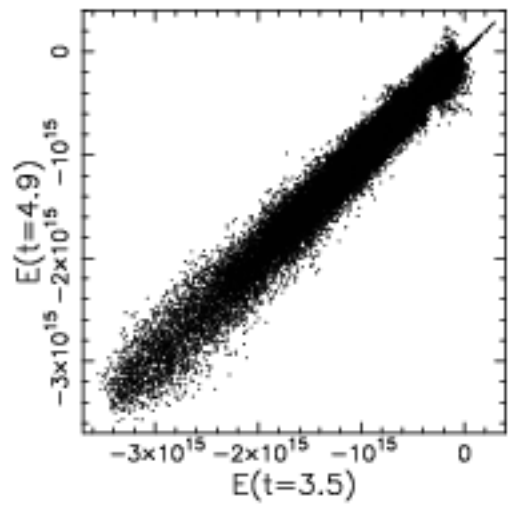

Figure 12. The energies $E = v^2/2 + \Phi$ of particles in the non-merger galaxy.

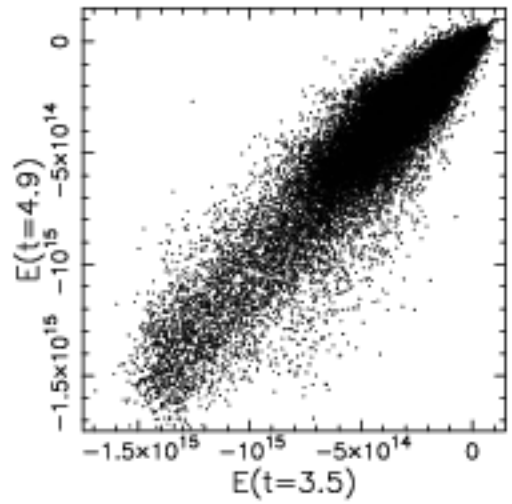

Figure 13. The energies of particles before and after the major merger at ~3.7 Gyr.

problem is not in magnitude, because the Faber–Jackson relation can be reproduced and the galaxy with given mass has reasonable luminosity. While the stellar mass-to-light ratio is consistent with the observation as $M/L_B \sim 5$–8, the total mass-to-light ratio is as large as $(M_{DM} + M_{baryon})/L \sim 10$–100 (within a sphere of $2r_s$), which may be too large. The baryon fraction increases to ~0.5 at the centre ($r < 1$ kpc) because of the stellar concentration, but is as small as ~0.2 in $r < 2r_s$. Baryon does not fully dominate even at the galaxy centre in our simulated galaxies and the stellar concentration seems to be insufficient compared with the dark matter concentration. These might be due to cosmological parameters, dynamical friction, the star formation parameter and the limited field size of the initial condition. As is well known with the zero-point offset in the Tully–Fisher relation (Navarro & Steinmetz 2000), such high dark matter concentration should arise from the standard CDM cosmology that is adopted in this paper and should decrease to some extent with the ΛCDM cosmology. However, Navarro & Steinmetz (2000) argued that the zero-point offset remains even with the ΛCDM cosmology, which requires substantial revision to the CDM

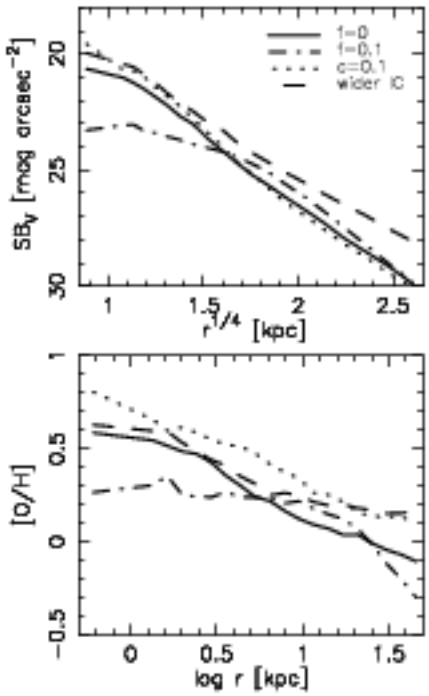

Figure 14. Surface brightness profiles (upper panel) and metallicity gradients (lower panel) with kinetic feedback (dash-dotted line, $f_{kin} = 0.1$), with a longer time-scale for the star formation (dotted line, $c = 0.1$) and a wider region of the initial condition (2.5 Mpc).

scenario such as σ_8, a tilt in the primordial power spectrum, or hot dark matter. The dynamical friction may be effective because the mass of a dark matter particle is 10 times larger than the gas and stellar particles (but see Steinmetz & White 1997). Too large an effective radius suggests that the star formation takes place too early before the gas accretes towards the centre. This can be solved by changing the star formation time-scale, i.e. reducing the star formation parameter c, although colours become bluer. As shown in Fig. 14, with $c = 0.1$ (dotted line), the surface brightness increases by 1 mag at the centre, which results in a smaller effective radius as $r_e = 3.2$ kpc. The metallicity increases because of the longer time-scale of star formation, but the gradient does not change as much. As mentioned in Section 3.2, the surface brightness profiles of our simulated galaxies follow the de Vaucouleurs law well, but are smeared out at the centre, and the central surface brightness ($r < 1$ kpc) is slightly smaller than the de Vaucouleurs fit (see Fig. 14). Although the resolution is not enough to discuss, this central stellar concentration may be smaller than other simulations (e.g. Springel & Hernquist 2003), can be as large with $c = 0.1$, and should be affected by the difference in the star formation and feedback schemes.

The initial condition is the most important. The edge of the simulated fields actually falls into a galaxy at $z \sim 2$–4 depending on the position of the galaxy in the field. The galaxy mass M_{200} (the mass with higher density than $200\rho_{crit}$) stops increasing at $z \sim 1.5$–3. This means that there is an artificial cut-off of mass accretion around this redshift, which results in the cut-off of star formation rate in Fig. 4. In a wider simulation with a radius of ~2.5 Mpc (dashed line in Fig. 14) instead of ~1.5 Mpc in the series of our simulation, the star formation continues longer, and thus colours tend to be too blue. The total luminosity becomes ~2 times larger, but still ~3 times smaller than the radius–magnitude relation. With much wider simulation, the

difference could be improved, but the colour inconsistency becomes much larger and such galaxy is no longer elliptical. The star formation and feedback schemes need to be modified accordingly, such as had been tried in some recent works (e.g. Springel & Hernquist 2003). In this paper, the mass accretion and star formation are truncated artificially by the initial condition. However, in observed ellipticals, star formation should be truncated at $z \sim 2$ by some process; such as tidal stripping, effects of active galactic nuclei, and so on. This epoch may correspond to the epoch when the galaxy falls into a cluster, because the galaxy moves too fast to cause mass accretion.

If we include the contribution of the outside of the simulated field, late accretion and late merging events should increase. Both make the metallicity gradient shallow. As noted in Section 2.3, fields with a larger spin parameter λ are not included in our simulation, and an elliptical can form through major mergers of disc galaxies in some such fields. However, as shown in Fig. 7, the predicted metallicity gradients are already in good agreement with the observation, and the increase of merger galaxies conflicts with the observation. If star formation and feedback schemes improved, evolution of metallicity gradients may also be affected to some extent. We should note, however, that the following conclusions will not change; major mergers make the metallicity gradients shallow and there should be non-merger ellipticals to explain the observed steep gradients.

5 CONCLUSIONS

We study the formation and evolution of galaxies with our GRAPE-SPH chemodynamical model that includes the various physical processes associated with the formation of stellar systems: radiative cooling, star formation, feedback from SNe II, SNe Ia and SWs, and chemical enrichment. We simulate 72 slowly rotating spherical fields (spin parameter $\lambda \sim 0.02$) and obtain 124 galaxies (78 ellipticals and 46 dwarfs) from the CDM initial fluctuation. All simulated galaxies have the de Vaucouleurs' surface brightness profiles, and are therefore elliptical galaxies. Most stars in ellipticals form during the initial starburst at $z \gtrsim 2$, while dwarfs undergo relatively continuous star formation. In our scenario, galaxies form through the successive merging of subgalaxies. The merging histories are various and the difference is seeded in the initial conditions. In some cases, galaxies form through the assembly of gas rich small galaxies and the process looks like a *monolithic collapse*. In other cases, the evolved galaxies undergo a *major merger* of galaxies. Major mergers are defined as those with the mass ratios of the primary and secondary galaxies being $f \gtrsim 0.2$.

We examine the physical conditions during 151 merging events that occur in our simulation. Whether the merging event changes the metallicity gradient is mainly influenced by two factors: the mass ratio of the merging galaxies f and the induced star formation. The basic processes of the formation and evolution of the gradients are summarized below.

(i) Formation of initial gradients. The initial gradient is determined from the initial starburst at $z \gtrsim 3$. The gradient is steeper in the case of quiescent gas accretion and is shallower in the case of violent assembly of subgalaxies. As a result, the initial gradients span from $\Delta[\mathrm{Fe/H}]/\Delta \log r = -1.5$ to -1.0.

(ii) Destruction by mergers. The major merger changes the orbits of stars. The metal-rich stars at the centre are able to move to the outer region of the galaxy. The gradient change is determined mainly from the mass ratio of merging galaxies f. With larger f, the gradients becomes shallower. If the mass ratio of merging galaxies is larger than $f \sim 0.2$, the gradient change is larger than ~ 0.5 dex.

(iii) Regeneration due to the induced star formation. If the ratio of gas mass is as large as $M_{\mathrm{g},2}/M_{\mathrm{g},1} \gtrsim 0.5$, strong star formation is induced at the centre of the primary galaxy, and the gradient change is smaller than ~ 0.5 dex.

(iv) Passive evolution. If the gas fraction of the secondary galaxy is larger than $f_{\mathrm{g},2} \sim 0.5$, moderate star formation is induced in the outer region of the primary galaxy and the gradient change becomes as large as ~ 0.5 dex, even if $f \sim 0$. In the case without a merging event, if a similar star formation is induced by the late gas accretion, the metallicity gradient gradually becomes shallower.

We succeed in reproducing the observations of metallicity gradients and finding the origin of the variety of internal structures. From the distribution functions of the gradients for different merging histories, we discuss the origin of elliptical galaxies.

(i) The average metallicity gradient is $\Delta \log Z/\log r \simeq -0.3$ and the dispersion is ± 0.2, which are both consistent with observations of Mg_2 gradients.

(ii) No correlation is produced between gradients and masses. The metallicity gradients do not depend on the galaxy mass and the variety of the gradients stems from the difference in the merging histories; galaxies that form monolithically have steeper gradients, while galaxies that undergo major mergers have shallower gradients.

(iii) The metallicity gradient distributions for (A) non-major merger (E1–3) and (B) major merger galaxies (E4, 5) are quite different. The typical gradients for non-major merger and major merger galaxies are $\Delta \log Z/\Delta \log r \sim -0.3$ and -0.2, respectively. Simulated galaxies with gradients steeper than -0.35 are all non-major merger galaxies.

The global properties of elliptical galaxies depend mainly on their masses, while their metallicity gradients are greatly affected by their merging history. A major merger makes the gradient shallower. Therefore, merging histories can be inferred from the observed metallicity gradients of present-day galaxies. Available observations for nearby galaxies suggest that there exist non-major merger galaxies and major merger galaxies half and half. The observed variation in the metallicity gradients cannot be explained by either *monolithic collapse* or by *major merger* alone. Instead, it is reproduced well in the present model in which both formation processes arise under the CDM scheme.

ACKNOWLEDGMENTS

This paper is a part of the PhD thesis of C. Kobayashi in the Astronomy Department of the University of Tokyo. I would like to thank the supervisor K. Nomoto and the advisor N. Arimoto. I am grateful to N. Nakasato, J. Makino, M. Mori, T. Kodama, N. Tamura, K. Ohta, V. Springel, F. van den Bosch and A. Renzini for fruitful discussions, and S.D.M. White for detailed suggestions. I also thank the Japanese Society for Promotion of Science for financial support, and the National Observatory of Japan for the GRAPE-5 MUV system.

REFERENCES

Abbott D.C., 1982, ApJ, 263, 723
Arimoto N., Yoshii Y., 1987, A&A, 173, 23
Bacon R. et al., 2001, MNRAS, 326, 23
Balakin D.S., 1995, J. Chem. Phys., 121, 357

Bagget A.J., Cowie L.L., Trentham N., Fulton E., Hu E.M., Songaila A., Hall D., 1999, AJ, 117, 102
Barnes J.E., 1988, ApJ, 331, 699
Barnes J.E., 1996, in Bender R., Davies R.L., eds, IAU Symp. 171, New Light on Galaxy Evolution. Kluwer, Dordrecht, p. 191
Baugh C.M., Cole S., Frenk C.S., 1996, MNRAS, 283, 1361
Bender R., Surma P., 1992, A&A, 258, 250
Benson A.J., Ellis R.S., Menanteau F., 2002, MNRAS, 336, 564
Benz W., Bowers R., Cameron A., Press W., 1990, ApJ, 348, 647
Bertschinger E., 1987, ApJ, 323, L103
Bertschinger E., 1995, http://arcturus.mit.edu/cosmics/
Bhanitov S., Lundqvist P., Baranov O., Nomoto K., Iwamoto K., 2000, ApJ, 532, 1132
Bower R.G., Lucey J.R., Ellis R.S., 1992, MNRAS, 254, 601
Brinchmann J., Ellis R.S., 2000, ApJ, 536, L77
Carlberg R.G., 1984, ApJ, 286, 403
Carollo C.M., Danziger I.J., Buson L., 1993, MNRAS, 265, 553
Carraro G., Lia C., Chiosi C., 1998, MNRAS, 297, 1021
Cimatti A. et al., 2002, A&A, 391, L1
Ciotti L., D'Ercole A., Pellegrini S., Renzini A., 1991, ApJ, 376, 380
Cole S., Aragón-Salamanca A., Frenk C.S., Navarro J.F., Zepf S.E., 1994, MNRAS, 271, 781
Cole S., Lacey C.G., Baugh C.M., Frenk C.S., 2000, MNRAS, 319, 168
Daddi E., Cimatti A., Renzini A., 2000, A&A, 362, L45
David L.P., Forman W., Jones C., 1990, ApJ, 459, 29
Davies R.L., Burstein D., Dressler A., Faber S.M., Lynden-Bell D., Terlevich R.J., Wegner G., 1987, ApJS, 64, 581
Davies R.L., Sadler E.M., Peletier R.F., 1993, MNRAS, 262, 650
de Vaucouleurs G., 1961, ApJS, 5, 233
Dickinson M., 1996, in Buzzoni A., Renzini A., Serrano A., eds, ASP Conf. Ser. Vol. 86, Fresh Views of Elliptical Galaxies. Astron. Soc. Pac., San Francisco, 283
Dickinson M., Papovich C., Ferguson H.C., Budavári T., 2003, ApJ, 587, 25
Djorgovski S., Davis M., 1987, ApJ, 313, 59
Dressler A., 1980, ApJ, 236, 351
Dressler A., Lynden-Bell D., Burstein D., Davies R.L., Faber S.M., Terlevich R.J., Wegner G., 1987, ApJ, 313, 42
Dressler A. et al., 1997, ApJ, 490, 577
Drory N., Bender R., Snigula J., Feulner G., Hopp U., maraston C., Hill G.J., Mendes de Oliveira C., 2001, ApJ, 562, L111
Efstathiou G., Davis M., Frenk C.S., White S.D.M., 1985, ApJS, 57, 241
Evrard A.E., 1988, MNRAS, 235, 911
Faber S.M., 1973, ApJ, 179, 731
Faber S.M., 1977, in Tinsley B.T., Larson R.B., eds, The Evolution of Galaxies and Stellar Populations. Yale University Press, New Haven, CT, p. 157
Forman A., Menci N., D'Odorico S., Ginolfo E., Poli F., Cristiani S., Moorwood A., Stanco P., 1999, MNRAS, 310, L27
Franceschini A., Silva L., Fasano G., Granato G.L., Bressan A., Arnouts S., Danese L., 1998, ApJ, 506, 600
Gingold R.A., Monaghan J.J., 1977, MNRAS, 181, 375
González J.J., Gregg J., 1996, in Buzzoni A., Renzini A., Serrano A., eds, ASP Conf. Ser. Vol. 86, Fresh Views of Elliptical Galaxies. Astron. Soc. Pac., San Francisco, 225
Gregg J., Efstathiou G., Aragón-Salamanca A., 1990, MNRAS, 245, 217
Gott J.R., 1973, ApJ, 186, 481
Gott J.R., 1975, ApJ, 201, 296
Greggio L., Renzini A., 1983, A&A, 118, 217
Habe A., Ohta K., 1992, PASJ, 44, 203
Hernquist L., Katz N., 1989, ApJS, 70, 419
Im M. et al., 2002, ApJ, 571, 136
Katz N., 1992, ApJ, 391, 502
Katz N., Weinberg D.H., Hernquist L., 1996, ApJS, 105, 19
Kauffmann G., 1996, MNRAS, 281, 487
Kauffmann G., Charlot S., 1998, MNRAS, 294, 705
Kauffmann G., White S.D.M., Guiderdoni B., 1993, MNRAS, 264, 201
Kawata D., Gibson B.K., 2003, MNRAS, 340, 908
Kelson D.D., van Dokkum P.G., Franx M., Illingworth G.D., Fabricant D., 1997, ApJ, 478, L13
Kennicutt R.C., Jr, 1983, ApJ, 272, 54
Kennicutt R.C., Jr, 1989, ApJ, 344, 685
Kobayashi C., 2002, PhD thesis, Univ. Tokyo
Kobayashi C., Arimoto N., 1999, ApJ, 527, 573
Kobayashi C., Tsujimoto T., Nomoto K., Hachisu I., Kato M., 1998, ApJ, 503, L155
Kobayashi C., Tsujimoto T., Nomoto K., 2000, ApJ, 539, 26
Kodama T., 1997, PhD thesis, Univ. Tokyo
Kodama T., Arimoto N., 1997, A&A, 320, 41
Kodama T., Arimoto N., Barger A.J., Aragón-Salamanca A., 1998, A&A, 334, 99
Larson R.B., 1974a, MNRAS, 166, 585
Larson R.B., 1974b, MNRAS, 169, 229
Larson R.B., 1975, MNRAS, 173, 671
Lattanzio C., Monaghan J., Pongracic H., Schwarz P., 1985, MNRAS, 215, 125
Leitherer C., Robert C., Drissen L., 1992, ApJ, 401, 596
Low C., Lynden-Bell D., 1976, MNRAS, 176, 367
Lucy L., 1977, AJ, 82, 1013
Lynden-Bell D., 1967, MNRAS, 136, 101
Marchant A.B., Shapiro S.L., 1977, ApJ, 215, 1
Matteucci F., 1996, Fundam. Cosmic Phys., 17, 283
Menanteau F., Ellis R.S., Abraham R.G., Barger A.J., Cowie L.L., 1999, MNRAS, 309, 208
Monaghan J.J., 1992, ARA&A, 30, 534
Monaghan J.J., Gingold R.A., 1983, J. Comput. Phys., 52, 374
Monaghan J.J., Lattanzio C., 1985, A&A, 149, 135
Moscardini M.B., Tissera P.B., Lambas D.G., Cora S.A., 2001, MNRAS, 325, 34
Nakamura N., 2000, PhD thesis, Univ. Tokyo
Nakamura N., Nomoto K., 2003, ApJ, 588, 842
Navarro J.F., Steinmetz M., 1997, ApJ, 478, 13
Navarro J.F., Steinmetz M., 2000, ApJ, 538, 477
Navarro J.F., White S.D.M., 1993, MNRAS, 265, 271
Navarro J.F., White S.D.M., 1994, MNRAS, 267, 401
Nomoto K., Thielemann F.-K., Yokoi K., 1984, ApJ, 286, 644
Nomoto K., Hashimoto M., Tsujimoto T. Thielemann F.-K., Kishimoto N., Kubo Y., Nakamura N., 1997a, Nucl. Phys., A, 616, 79c
Nomoto K., Iwamoto K., Nakamura N., Thielemann F.-K, Brachwitz F., Tsujimoto T., Kubo Y., Kishimoto N., 1997b, Nucl. Phys., A, 621, 467c
Raiteri C.M., Villata M., Navarro J.F., A&A, 315, 105
Renzini A., 2002, in Fusco-Femiano R., Matteucci F., eds, ASP Conf. Ser. Vol. 253, Chemical Enrichment of Intracluster and Intergalactic Medium. Astron. Soc. Pac., San Francisco, p. 331
Salpeter E.E., 1955, ApJ, 121, 161
Schade D., Barrientos L.F., Lopez-Cruz O., 1997, ApJ, 477, L17
Schade D. et al., 1999, ApJ, 525, 31
Schmidt M., 1959, ApJ, 129, 243
Schweizer F., Seitzer P., 1992, AJ, 104, 1039
Schweizer F., Seitzer P., Faber S.M., Burstein D., Dce C.M.D., Gonzalez J.J., 1990, ApJ, 364, L33
Silk J., 1977, ApJ, 214, 718
Silva D.R., Bothun G.D., 1998, AJ, 116, 85
Springel V., Hernquist L., 2003, MNRAS, 339, 289
Stanford S.A., Eisenhardt P.R.M., Dickinson M., 1998, ApJ, 492, 461
Steinmetz M., 1996, MNRAS, 278, 1005
Steinmetz M., Müller E., 1994, A&A, 281, L97
Steinmetz M., Navarro J.F., 2002, New Astron., 7, 155
Steinmetz M., White S.D.M., 1997, MNRAS, 288, 545
Sugimoto D., Chikada Y., Makino J., Ito T., Ebisuzaki T., Umemura M., 1990, Nat, 345, 33
Sutherland R.S., Dopita M.A., 1993, ApJS, 88, 235
Thomas P.A., Couchman H.M.P., 1992, MNRAS, 257, 11
Tinsley B.M., 1980, Fundamentals of Cosmic Physics Vol. 5, p. 287

Toomre A., 1977, in Tinsley B.M., Larson R.B., eds, The Evolution of Galaxies and Stellar Populations. New Haven, Yale Univ. Observatory, p. 401
Toomre A., Toomre J., 1972, ApJ, 178, 623
Tripicco M.J., Bell R.A., 1995, AJ, 110, 3035
Umemura M., Fukushige T., Makino J., Ebisuzaki T., Sugimoto D., Turner E., Loeb A., 1993, PASJ, 45, 311
van Albada T.S., 1982, MNRAS, 201, 939
van Dokkum P.G., Franx M., 1996, MNRAS, 281, 985
van Dokkum P.G., Franx M., 2001, ApJ, 553, 90
Warren M.S., Quinn P.J., Salmon J.K., Zurek W.H., 1992, ApJ, 399, 405
White S.D.M., 1978, MNRAS, 184, 185
White S.D.M., 1980, MNRAS, 191, 1p
Woosley S.E., Weaver T.A., 1995, ApJS, 101, 181
Zel'dovich Ya. B., 1970, A&A, 5, 84
Zepf S.E., 1997, Nat, 390, 377

This paper has been typeset from a TEX/LATEX file prepared by the author.